

1 Simultaneous solution for mass trends on the West Antarctic Ice Sheet

2
3 N.Schoen¹, A. Zammit-Mangion^{1,2}, J. C. Rougier², T. Flament³, F. Rémy⁴, S. Luthcke⁵, J. L.
4 Bamber¹

5
6 [1] {Bristol Glaciology Centre, School of Geographical Sciences, University of Bristol, UK}

7 [2] {Department of Mathematics, University of Bristol, UK}

8 [3] {School of Earth and Environment, University of Leeds, UK}

9 [4] {LEGOS, Toulouse, France}

10 [5] {NASA, Greenbelt, MD, USA}

11 Correspondence to: Jonathan Bamber (j.bamber@bristol.ac.uk)

12 13 Abstract

14 The Antarctic Ice Sheet is the largest potential source of future sea-level rise. Mass loss has been
15 increasing over the last two decades for the West Antarctic Ice Sheet (WAIS), but with significant
16 discrepancies between estimates, especially for the Antarctic Peninsula. Most of these estimates
17 utilise geophysical models to explicitly correct the observations for (unobserved) processes.
18 Systematic errors in these models introduce biases in the results which are difficult to quantify. In
19 this study, we provide a statistically rigorous, error-bounded trend estimate of ice mass loss over
20 the WAIS from 2003–2009 which is almost entirely data-driven. Using altimetry, gravimetry, and
21 GPS data in a hierarchical Bayesian framework, we derive spatial fields for ice mass change,
22 surface mass balance, and glacial isostatic adjustment (GIA) without relying explicitly on forward
23 models. The approach we use separates mass and height change contributions from different
24 processes, reproducing spatial features found in, for example, regional climate and GIA forward
25 models, and provides an independent estimate, which can be used to validate and test the models.
26 In addition, spatial error estimates are derived for each field. The mass loss estimates we obtain
27 are smaller than some recent results, with a time-averaged mean rate of -76 ± 15 Gt/yr for the
28 WAIS and Antarctic Peninsula (AP), including the major Antarctic Islands. The GIA estimate
29 compares well with results obtained from recent forward models (IJ05-R2) and inverse methods
30 (AGE-1). The Bayesian framework is sufficiently flexible that it can, eventually, be used for the
31 whole of Antarctica, can be adapted for other ice sheets and can utilise data from other sources
32 such as ice cores, accumulation radar data and other measurements that contain information about
33 any of the processes that are solved for.

34 1 Introduction

35 Changes in mass balance of the Antarctic ice sheet have profound implications on sea level. While
36 there is a general consensus that West Antarctica has experienced ice loss over the past two
37 decades, the range of mass-balance estimates still differ significantly (compare, for example,
38 estimates in Shepherd et al. (2012), Tables S8 and S11 which range from -84 ± 18 for GRACE to -

39 13 ± 39 Gt yr⁻¹ for ICESat for the WAIS and from -24 ± 35 to 123 ± 60 for the East Antarctic Ice
40 Sheet).). Reconciling these disparate estimates is an important problem. Previous studies have
41 made use of satellite altimetry (Zwally et al 2005), satellite gravimetry (Chen et al., 2006; King et
42 al., 2012; Sasgen et al. 2013; Luthcke et al., 2013), or a combination of satellite and airborne data
43 and climate model simulations (Rignot et al., 2011) to provide estimates. In the latter case, the
44 balance is found by deducting output ice flux from input snowfall in a technique sometimes
45 referred to as the Input-Output Method (IOM) or mass budget method.

46 Different approaches have different sources of error. A key error in the gravimetry-based
47 estimates is a result of incomplete knowledge on glacial isostatic adjustment (GIA), which
48 constitutes a significant proportion of the mass-change signal but leakage and GRACE errors are
49 also important (Horwath and Dietrich, 2009)(. For satellite altimetry, uncertainties arise from
50 incomplete knowledge of the temporal variability in precipitation (Lenaerts et al.,2012, Frezzotti
51 et al.,2012), and the compaction rates of firn (Arthern et al., 2010, Ligtenberg et al., 2011):
52 quantities which play a central rôle in determining the density of the observed volume change. For
53 the IOM, the main sources of errors stem from the surface mass balance (SMB) estimates used
54 (obtained from a regional climate model), and uncertainties in ice discharge across the grounding
55 line. Recent improvements in regional climate modelling have reduced the uncertainty in the SMB
56 component but differences between estimates for the Antarctic ice sheet as a whole still exceed
57 recent estimates of its mass imbalance. For example, a recent update of the commonly used
58 regional climate model, RACMO, has resulted in a change in the integrated ice sheet-wide SMB
59 of about 105 Gt yr⁻¹ (Van Wessem et al, 2014), which is larger than most recent estimates of the
60 ice sheet imbalance. This change in SMB, directly impacts the IOM estimate by the same amount.
61 It is these hard-to-constrain biases in the forward models, such as the one just described, that has,
62 in part, motivated our approach..

63 In an attempt to reduce the dependency on forward models, recent studies have combined
64 altimetry and GRACE to obtain a data-driven estimate of GIA and ice loss simultaneously (Riva
65 et al.,2009, Gunter et al.,2013). Here, we extend these earlier approaches in a number of ways. We
66 provide a model-independent estimate not only of GIA, but also of the SMB variations, firn
67 compaction rates and of the mass loss/gain due to ice dynamics (henceforward simply referred to
68 as ice dynamics). In doing so, we eliminate the dependency of the solution on solid-Earth and
69 climate models. The trends for ice dynamics, SMB, GIA, and firn compaction are obtained
70 independently through simultaneous inference in a hierarchical statistical framework. The climate
71 and firn compaction forward models are used solely to provide prior information about the spatial
72 smoothness of the SMB-related processes. Systematic biases in the models have, therefore,
73 minimal impact on the solutions. In addition, we employ GPS bedrock uplift rates to further
74 constrain the GIA signal. In future work the GPS data will also be used to constrain localised ice
75 mass trends that cause an instantaneous elastic response of the lithosphere (Thomas and King
76 (2011). The statistical framework uses expert knowledge about smoothness properties of the
77 different processes observed (i.e. their spatial and temporal variability) and provides statistically
78 sound regional error estimates that take into account the uncertainties in the different observation
79 techniques (Zammit-Mangion et al. 2014). The study reported here was performed as a proof-of-
80 concept for a time-evolving version of the framework for the whole Antarctic ice sheet, which is

81 currently under development. The time-evolving solution will use updated data sets and, as
 82 explained above, will also solve for the elastic signal in the GPS data. In addition, it will provide
 83 improved separation of the processes because of the additional information related to temporal
 84 smoothness that can be incorporated into the framework (discussed further in section 5).

85

86 **2 Data**

87 In this section we describe the data employed, which is divided into two groups. The first group
 88 contains observational data which play a direct rôle in constraining the mass trend. These include
 89 satellite altimetry, satellite gravimetry and GPS data (Sections 2.1–2.3). The second group
 90 comprises auxiliary data (both observational and data extracted from geophysical models), which
 91 we use to help with the signal separation (differentiating between the different processes we solve
 92 for accounting for their spatial smoothness) (Zammit-Mangion et al. 2014). These are discussed in
 93 Section 2.4.

94 **2.1 Altimetry**

95 We make use of two altimetry data sets in this study, obtained from the Ice, Cloud and land
 96 Elevation Satellite (ICESat) and the Environment Satellite (Envisat). In this study, we used ICESat
 97 elevation rates (dh/dt) based on release 33 data from February 2003 until October 2009 (Zwally et
 98 al., 2011). The data includes the “86S” inter-campaign bias correction presented in Hofton et al.,
 99 2013) and the centroid Gaussian correction (Borsa et al., 2013) made available by the National
 100 Snow and Ice Data Centre. Pre-processing was carried out as described in Sørensen et al., 2011).
 101 Since ICESat tracks do not precisely overlap, a regression approach was used for trend extraction,
 102 in which both spatial slope (both across-track and along-track) and temporal slope (dh/dt) were
 103 simultaneously estimated (Howat et al., 2008), Moholdt et al., (2010). A regression was only
 104 performed if the area under consideration, typically 700m long and a few hundred metres wide,
 105 had at least 10 points from four different tracks that span at least a year. Regression was carried
 106 out twice, first to detect outliers (data points which lay outside the 2σ confidence interval), and
 107 second to provide a trend estimate following outlier omission. The standard error on the
 108 regression coefficient (in this case dh/dt), SE_{coef} , was calculated through (Yan (2009):

$$109 \quad SE_{coef} = \frac{1}{\sqrt{n-2}} \sqrt{\frac{\sum_i e_i^2}{\sum_i (x_i - \bar{x})^2}} \quad (1)$$

110 where $e = [e_i]$ is the vector of residuals, n is the sample size, and $x = [x_i]$ is the input with mean \bar{x} .
 111 It should be noted that this standard error is not equivalent to the measurement error, but takes
 112 into account sample size, as well as the variance of both input data and residuals of the regression.
 113 Only elevation changes with an associated standard error on dh/dt of less than 0.40m/yr were
 114 considered. The 0.40m/yr threshold was selected by trial and error to avoid a noisy spatial pattern
 115 of points that are close together and opposite in sign, usually because the regression is based on a
 116 small subset of overpasses. Data above the latitude limit of 86° S were omitted. The remaining
 117 data were gridded on a polar-stereographic projection (central latitude 71° S; central longitude
 118 0° W, and origin at the South Pole), at a 1 km resolution and then averaged over a 20km grid. The

119 error used in the modelling framework was then the spread (standard deviation) of the trends
120 within each 20km grid box, as in Riva et al., 2009). The Envisat mission data began in September
121 2002 and ended in April 2012. Compared to laser altimetry, radar altimetry is, in general, less
122 suited for measurements over ice for several well-known reasons: the large spatial footprint, the
123 relatively poor performance in steeper-sloping marginal areas (Thomas et al., 2008), and the
124 variable snow-pack radar penetration (Davis, 1996). On the other hand Envisat data exhibit better
125 temporal and spatial coverage over much of the WAIS, primarily because of the instrument issues
126 associated with ICESat that resulted in a shorter repeat cycle and less frequent operation than
127 originally planned. We use the along-track dh/dt trends presented in Flament et al., 2012), which
128 were obtained by binning all points within a 500m radius and then fitting a 10-parameter least-
129 squares model in order to simultaneously correct for across-track topography, changes in
130 snowpack properties and dh/dt . The re-trended residuals were then used to obtain linear trends
131 over the 2003–2009 ICESat period for our study. As with ICESat, the data were averaged over a
132 20km grid and the standard deviation of the trends were used as the error at this scale.

133 **2.2 GRACE**

134 The Gravity Recovery and Climate Experiment (GRACE, Tapley et al., 2005) has provided
135 temporally continuous gravity field data since 2002. Different methods have been used to provide
136 mass change anomalies from the Level 1 data. Most are based on the expansion of the Earth's
137 gravity field into spherical harmonics; but to make the data usable for ice mass change estimates,
138 it is generally necessary to employ further processing methods. These include the use of averaging
139 kernels (Velicogna et al., 2006), inverse modelling (Wouters et al., 2008), Sasgen et al., 2013),
140 and mass concentration (mascon) approaches (Luthcke et al., 2008). Spherical harmonic solutions
141 usually depend on filtering to remove stripes caused by correlated errors (Kusche et al., 2009),
142 Werth et al., 2009).

143 In this paper, we used a release of mascon solutions (Luthcke et al., 2013), although we stress that
144 the framework is not limited to this class of solutions. The mascon approach employed here
145 directly uses the GRACE K-band inter-satellite range-rate (KBRR) data which are then binned
146 and regularized using smoothness constraints. The release 4 (RL4) Atmosphere/ Ocean model
147 correction, which utilizes the European Centre for Medium-Range Weather Forecasts
148 atmospheric data and the Ocean Model for Circulation and Tides (OMCT), was used (Dobslaw
149 and Thomas (2007). Some concerns with this correction have been reported (Barletta et al., 2012),
150 but a release of the mascon data using the corrected version (Dobslaw et al., 2013) was not
151 available for this study. Contributions to degree-one coefficients were provided using the
152 approach by Swenson et al., 2008). The mascon approach used here does not call for a
153 replacement of C20 coefficients. We assume that GRACE does not observe SMB or ice mass
154 changes over the floating ice shelves as they are in hydrostatic equilibrium). Hence, all observed
155 mass changes over the ice shelves are assumed to be caused by GIA.

156 Although the mascons are provided at a resolution of about 110km, their fundamental resolution is
157 nearer that of the original KBRR data (~300km, Luthcke et al., 2013). For the statistical
158 framework, it is important to quantify the correlation among the mascons so that it is taken into
159 account when inferring both the processes and associated uncertainties. We quantify the spatial

160 correlation by determining an averaging model such that the diffused signal is able to loosely
161 reconstruct the mass loss obtained using only altimetry (and assuming that all height change
162 occurs at the density of ice). The averaging strength between mascon neighbours is also estimated
163 during the inference (Zammit-Mangion et al., 2014). The error on the mascon rates is assumed to
164 be a factor of the regression residuals on the trends, in a similar manner to the altimeter data
165 (Zammit-Mangion et al. 2014)The a-priori errors, after these two steps, are shown in Figure 1,
166 which also indicates the length-scale over which we estimated the GRACE mascons to be
167 uncorrelated.

168 **2.3 GPS**

169 The GPS trends used in this work were taken from Thomas and King (2011). Not all of the trends
170 were suitable for our analysis, as the length of record did not always coincide with the 2003–2009
171 ICESat period. We only used stations with contemporaneous data, as well as those where we
172 could access the original time series to confirm that the trend had stayed the same, within the error
173 bounds, for our observation period. For the North Antarctic Peninsula, we followed the approach
174 suggested in Thomas and King (2011) and used the pre-2003 trends, ignoring the later trend
175 estimates which are strongly influenced by elastic signals. All other stations were corrected for
176 elastic rebound as in Thomas & King (2011) and subsequently assumed to be measuring GIA only
177 (the published rates were used). A more advanced approach where the estimated ice loss is fed
178 back into a dynamic estimate of the elastic rebound, is being implemented for a spatiotemporal
179 extension of the Bayesian framework. The GPS data used in this study are detailed in Table 1.

180 **2.4 Additional data sets**

181 **RACMO.** Elements of the Regional Atmospheric Climate Model version 2.1 (RACMO, Lenaerts
182 et al., 2012) were used to constrain SMB properties. Spatially-varying length scales describing
183 spatial smoothness of precipitation patterns were obtained from the 2003–2009 SMB anomalies
184 (with respect to the 1979–2002 mean). These ranged from 80km in the Antarctic Peninsula to
185 200km east of Pine Island Glacier. The amplitude of the anomalies, which peaked at 50 mm water
186 equivalent in the Antarctic Peninsula, was used to provide the order of magnitude annual
187 amplitudes for expected regional SMB variability (Zammit-Mangion et al. 2014)et al., .
188 RACMO2.1 also provides a surface density map: the mean annual density of the surface layer.
189 This was used to translate height changes corresponding to the SMB field to mass changes.

190 **Firn correction.** We used the firn correction anomalies for 2003–2009 (with respect to the 1979–
191 2002 mean) from a firn compaction model (Ligtenberg et al., 2011). These anomalies were used
192 to estimate, empirically, the correlation between firn compaction rate and surface mass balance.
193 This relationship was then subsequently used to determine jointly the SMB and firn correction
194 processes, subject to the constraint that firn compaction is a linear function of SMB (supported by
195 the high correlation between the respective 2003–2009 trends). The methodology automatically
196 takes into account inflated uncertainties due to confounding of these two processes (since they
197 have identical length scales), (Zammit-Mangion et al. 2014).

198 **Ice Velocities.** We use surface ice velocities derived from Interferometric Synthetic Aperture
199 Radar (InSAR, Rignot (2011) data. In places where no observational data were available,
200 theoretical balance velocities (Bamber (2000) were used. This composite velocity field was
201 employed to help in the separation of signals due ice dynamics versus those due to SMB (Section
202 3).

203 **3 Methodology**

204 Our statistical framework makes use of several recent improvements in statistical modelling
205 which can be exploited for geophysical purposes. Complete details regarding the mathematical
206 methods employed are given in (Zammit-Mangion et al., 2014) and here, we provide a conceptual
207 overview of the approach. A description of the software implementation can also be found in
208 Zammit et al, (2015). The statistical framework hinges on the use of a hierarchical model where
209 the hierarchy consists of three layers, the observation layer (which describes the relation of the
210 observations to the measured fields), the process layer (which contains prior beliefs of the fields
211 using auxiliary data sets) and the parameter layer (where prior beliefs over unknown parameters
212 are described).

213 The ‘observation model’ is the probabilistic relationship between the observed values and the
214 height change of the each of the processes. For point-wise observations, such as altimetry and
215 GPS, the observations were assumed to be measuring the height trend at a specific location.
216 GRACE mascons, on the other hand, were assumed to represent integrated mass change over a
217 given area. These mass changes were translated into height changes via density assumptions:
218 upper mantle density was fixed at 3800 kg/m^3 ; ice density at 917 kg/m^3 , and SMB at values
219 ranging from $350\text{-}600 \text{ kg/m}^3$. Recall (Section 2.4) that we used the density map from Ligtenberg
220 et al., 2011) to specify the density of the surface layer.

221 In the ‘process model’ four fields (or latent processes) are modelled: ice dynamics, SMB, GIA,
222 and a field which combines the processes which result in height changes, but no mass changes:
223 firm compaction and elastic rebound. We model the height changes due to these as spatial
224 Gaussian processes, i.e. we assume that they can be fully characterised by a mean function and a
225 covariance function. For each field we assume that the mean function is zero (we do not use
226 numerical models to inform the overall mean) and that the covariance function, which describes
227 how points in space covary, is highly informed by numerical models and expert knowledge as
228 described next. The relationship between the observations, priors and the latent process, defined
229 by the process model is shown schematically in Figure 2. Those processes that are influenced by
230 an observation are linked by a solid arrow and it is evident that the problem is underdetermined as
231 there are less independent observations than there are latent processes. This is why the use of
232 priors is important and useful for source separation (i.e. for partitioning elevation change between
233 the four latent processes shown in Figure 2). It should also be noted that SMB and firm
234 compaction have been assumed, in this implementation of the framework, to covary *a priori*, as
235 discussed later.

236 The practical spatial range of surface processes – this describes the distance beyond which the
237 correlation drops to under 10% – was estimated from RACMO2.1 as described in Section 2.4.

238 This analysis revealed, for example, that locations at 100km are virtually uncorrelated in the
 239 Antarctic Peninsula, but highly correlated East of Thwaites. Similarly GIA was found to have a
 240 large practical range (~3000 km), from an analysis of the IJ05-R1 model(although version R2 is
 241 used for comparison in the results and discussion) et al.,). These length scales impose soft
 242 restrictions on the possible class of solutions for the individual fields. They are useful, however,
 243 for helping to partition a height change between the different processes that can cause that change.
 244 For example, a long wavelength variation in height that spans different basins is likely associated
 245 with SMB, whereas a localised change that shows some relationship to surface velocity is likely
 246 associated with ice dynamics (Hurkmans et al., 2014). Hence, mass loss due to ice dynamics was
 247 assumed to mostly take place in areas of faster flow (Hurkmans et al., 2014). A “soft” constraint
 248 was thus placed on elevation rates due to ice dynamics such that it is small (1mm/yr) at areas of
 249 low velocities and can be large (up to 15m/yr) at velocities greater than 10m/yr. A sigmoid
 250 function was used to describe this soft constraint:

$$251 \quad \sigma_{vel}(\mathbf{s}) = \frac{15}{1+\exp(-(v(\mathbf{s})-10))} \quad (2)$$

252 where $v(\mathbf{s})$ denotes the horizontal velocity at location \mathbf{s} . For illustration of how $\sigma_{vel}(\mathbf{s})$ is used, an
 253 altimetry elevation trend of 10m/yr in Pine Island Glacier where velocities exceed 4 km/yr is
 254 within the $1\sigma_{vel}$ interval and thus classified as “probable”. On the other hand, a 10m/yr trend in a
 255 region east of Thwaites, where velocities are 2m/yr, would lie within the $2000\sigma_{vel}$ level and thus
 256 assumed to be a virtually impossible occurrence *a priori*. At Kamb ice stream, this assumption
 257 had to be relaxed as this area shows thickening from the shutdown of Kamb ice Stream about 150
 258 years ago (Retzlaff and Bentley, 1993). Although the velocity of the ice is low, the thickening
 259 occurs at relatively high rates. To reflect this, we fix $\sigma_{vel}(\mathbf{s}) = 2\text{m/yr}$ in this drainage basin. In
 260 Table 2, we outline the key length-scale and amplitude constraints placed on the fields that are
 261 solved for in the framework. These soft constraints should be seen as ones characterising the
 262 solution in the absence of strong evidence to anything otherwise. They can be ‘violated’ if the data
 263 is sufficiently informative. In the Discussion we examine the sensitivity of the solution to these
 264 constraints.

265 Length scales and prior soft constraints are easily defined for Gaussian processes (or Gaussian
 266 fields) which, on the other hand, are also computationally challenging to use. Gaussian fields can
 267 however be re-expressed as Gaussian Markov Random Fields (GMRF) by recognising that
 268 Gaussian fields are in fact solutions to a class of Stochastic Partial Differential Equations (SPDEs,
 269 Lindgren et al., 2011). Numerical methods for partial differential equations, namely, finite
 270 element (FE) methods, can thus be applied to the SPDEs in order to obtain a computationally
 271 efficient formulation of a complex statistical problem (Zammit-Mangion et al., 2014). Spatially
 272 varying triangulations (meshes) are used for the different processes reflecting the assumption that,
 273 for example, ice loss is more likely to occur at smaller scales near the margins of the ice sheet
 274 where fast, narrow ice streams are prevalent, than in the interior. We thus use a fine mesh at the
 275 margins (25km) and a coarse mesh in the interior for this field. GIA on the other hand is assumed
 276 to be smooth. This allows us to use a relatively coarse mesh for this process (~100km).

277 We note that our methodology differs from others in that it is not an unweighted average of
278 estimates with markedly different errors (Shepherd et al., 2012) or a sum of corrected data sources
279 (Riva et al., 2009), but a process-based estimate. For each of the four fields (noting that elastic
280 rebound and firn compaction covary in this implementation), we infer a probability distribution
281 and standard deviation for every point in space. By relating pre-inference and post-inference
282 variances, it is possible to assess the influence of different kinds of observation at each point on
283 the resulting fields.

284 4 Results

285 Inferential results are available for of the three processes shown in Figure 2 in isolation. In this
286 section we report the results for each of the processes in turn, but emphasise that these are
287 presented to demonstrate the methodology rather than provide final estimates. This is because, as
288 stated in section 2, improvements are planned both to the framework and the data sets that we use
289 in it. In all the examples shown, green stippling indicates where the signal is greater than marginal
290 standard deviation.

291 **Ice dynamics.** We obtain an ice dynamics imbalance of -86.25 ± 16.12 Gt/yr. The results for ice
292 dynamics (Fig. 3a) are consistent with prior knowledge of disequilibria in ice flow in the West
293 Antarctic Ice Sheet (WAIS), for example, the ice build-up in the Kamb Ice Stream catchment
294 (Retzlaff and Bentley, 1993) and the wastage in the Amundsen Sea Embayment (Flament et al.,
295 2012). The strength of the approach is apparent when focusing on the Antarctic Peninsula (Fig.
296 3b). Due to the relatively narrow, steep terrain, and northern latitude (which affects the across
297 track spacing of the altimetry) satellite altimeter data are sparse, while GRACE data are strongly
298 affected by leakage effects, making it challenging to localise the mass sources and sinks. We find
299 that the framework places ice loss maxima at the outlets of several glaciers and ice streams, which
300 are known to have accelerated (De Angelis and Skvarca, 2003). The result is a high-resolution
301 map of ice mass loss or gain that can be linked to specific catchments. Strong ice loss can be
302 observed on the Northern Peninsula at the Weddell Sea shore, at the former tributaries of the
303 Larsen B ice shelf. The maximum ice loss rate is found in the area around Sjögren Glacier with -
304 4.7m/yr. Neighbouring Röhss Glacier, on James Ross Island, has been thinning considerably since
305 the break-up of the Prince Gustav Ice Shelf (Glasser et al. 2011, Davies et al. 2011). This is also
306 reflected in high loss rates. Hektoria and Evans, Gregory Glacier, and glaciers the Philippi Rise
307 also show strong ice mass loss signals, most likely as a result of the collapse of the Larsen B ice
308 shelf (Scambos et al., 2004, Berthier et al., 2012). Other ice loss maxima are found in the region
309 of the Wordie Ice Shelf (see Fig. 10 for reference), Marguerite Bay, and Loubet Coast, which
310 corroborates findings from USGS/BAS and ASTER airborne stereo imagery analyses (Kunz et al.,
311 2012). Ice loss is also observed on King George Island, which is in agreement with recent
312 analyses of satellite SAR data (Osmanoğlu et al., 2013), and on Joinville Island. Ice build-up is
313 observed over the Southern Peninsula (Kunz et al., 2012).

314 The gap in altimeter data around the pole results in spurious estimates for that region and the
315 shaded area, south of 86° , is not considered here. As expected, the marginal standard deviation, or
316 error estimate, (Fig. 4) is lowest in the interior of the WAIS, where sampling density by altimetry
317 is high, and highest on the Peninsula, where data are sparse. Also, steep coastal areas show larger

318 errors, reflecting the dependency of altimeter errors on slope (see Bamber et al., 2005) or Brenner
319 et al., 2007).

320 **SMB and firn compaction.** We obtain an SMB imbalance of 10.57 ± 4.98 Gt/yr. Fig. 5 shows the
321 trend of the cumulative SMB anomalies according to RACMO 2.1, calculated with respect to the
322 1979–2010 mean. This approximately corresponds to the signal we are estimating, since we are
323 only considering trends with respect to a steady state SMB. A cursory inspection of the anomalies
324 we obtain (Fig 6) with those from RACMO2.1 (Fig 5) suggests relatively poor agreement. It
325 should be noted, however, that the anomalies over the seven year interval are on the order of a few
326 centimetres a year and only a limited area has a statistically significant trend in our inversion
327 (stippled regions in Fig 6). There is a difference in sign between the model and our inversion for
328 the Northern Antarctic Peninsula but again, the rates we obtain are below a significant threshold
329 and the Peninsula possesses larger uncertainties than other areas for both our framework and the
330 regional climate model. In Fig. 7, we compare our results with ice core trends from Medley et al.
331 (2013) who conclude that, while in phase, RACMO2.1 appears to show exaggerated inter-annual
332 variability in the Amundsen Sea Sector. The ice core trend labeled ‘MEDLEY’ is the mean of
333 three cores PIG2010, THWAITES2010, and DIV2010 collected in 2010; the location in Fig. 7 is,
334 consequently, the mean coordinates for all the cores. The trends at the single ice cores were not
335 listed, but there appears to be qualitative agreement with our negative trend in the area. Burgener
336 et al. (2013) also provide new ice core records for the Amundsen Sea sector (Satellite Era
337 Accumulation Traverse, SEAT) and Fig. 7 also shows a comparison with their data. Trends were
338 taken over the full 2003–2009 period relative to a mean for 1980–2009. The agreement is good for
339 three out of five cores given in the paper. Following Burgener et al. (2013), we exclude SEAT 10-
340 4 because of the high noise level in the isotope dating and surface undulations. SEAT10-5 shows a
341 relatively strong negative trend that we do not reproduce. SEAT-01, SEAT-03, and SEAT-06
342 agree well with our results at the \pm cm yr⁻¹ level. We note, however, that there is substantial short-
343 wavelength spatial variability in SMB based on the ice core data, which is below the resolution of
344 our framework. This also suggests that a single ice core measurement should be treated with
345 caution in this type of comparison.

346 Height changes from firn compaction and elastic rebound are estimated together in a single field.
347 Because they take place on similar length scales, and there is no temporal evolution in our time-
348 invariant solution presented here, they are confounded in this study. Since firn compaction occurs
349 at relatively large rates (cm a⁻¹), we cannot make any useful inferences about elastic rebound rates.
350 We expect this issue to be less critical in the time-evolving version of the framework. The
351 modelled inverse correlation between firn compaction and SMB (Section 2.4) is visible in the
352 results (Fig. 6 and Fig. 8).

353 **GIA.** We obtain a GIA rate that is equivalent to a mass trend of 12.34 ± 4.32 Gt/yr. It is difficult
354 to compare this directly with other published results because the domain is not the same. We do,
355 however, examine individual basins. The GIA vertical velocities estimated by our framework are
356 lower than some older forward model solutions (e.g. Peltier (2004), Ivins and James (2005)). Our
357 results, however, agree well with a recent GRACE-derived estimate, AGE-1, which also assumes
358 that over the ice shelves, GIA is the sole process causing observed mass change (Sasgen et al.,
359 2013). Compared with AGE-I, our maxima in vertical uplift are shifted towards the open ocean

360 for both of the major ice shelves (Fig. 9). Agreement with the trends at most GPS stations is good;
361 however, the imposed smoothness constraints have a larger influence. The W06A station (Table
362 1), which has a strong negative trend with a large error, exacerbated by a strong elastic signal,
363 stands out. Thomas and King (2011) show that its rate does not fit with any of the GIA models
364 used in their comparison. The signal is effectively ignored in our framework due to the large
365 spatial scale assumed for the GIA process.

366 In Fig. 12, we compare our results (denoted 'RATES') with basin estimates from AGE-1 (Sasgen
367 et al., 2013), two recent forward models, W12a (Whitehouse et al., 2012) and IJ05-R2 (Ivins et
368 al., 2013), and a data-driven inversion by Gunter et al. (2013) (denoted 'Gunter13'), which is an
369 update of Riva et al. (2009). Basin definitions are shown in Fig. 11. Both Gunter13 and AGE-1
370 rely on GRACE data. W12a, while a forward model, was adjusted to better match GPS uplift rates
371 on the Peninsula. In general, over the domain covered in this study, we obtain closest agreement
372 with the AGE-1 solution. For the Filchner Ronne Ice Shelf (basin 1), the AGE-1 estimate (2.1
373 mm/yr) is slightly lower than ours (2.7 mm/yr), while IJ05-2 is slightly higher (3.5 mm/yr). W12a
374 (7.2 mm/yr) shows more than twice our rate in this area, while Gunter13 (4.2 mm/yr) lies between
375 IJ05-R2 and W12a. At the Ross Ice Shelf (basin 18), the agreement with AGE-1 and IJ05-R2
376 (both 1.9 mm/yr, RATES 2.0 mm/yr) is very close. Gunter13 (3.1 mm/yr) and W12a (3.4 mm/yr)
377 are slightly higher. For basin 19, again the agreement with AGE-1 and IJ05-R2 is close with
378 RATES at 2 mm/yr, AGE-1 at 1.7 mm/yr and IJ05-R2 at (1.9 mm/yr). Gunter13 and W12a are,
379 again, somewhat higher here, at 2.6 mm/yr and 2.7 mm/yr, respectively. All model estimates lie
380 within our error bounds.

381 Basin 20 lies between the Ross Ice Shelf region and the Amundsen Sea sector. Here, our uplift
382 rate (1.1 mm/yr) lie closest to IJ05-2 (0.9 mm/yr), with AGE-1 at 0.5 mm/yr and W12a at 1.8
383 mm/yr. Gunter13 has the highest rate (2.2 mm/yr) for this basin. Basins 21 and 22 extend to the
384 Amundsen Seas Sector, one of the most rapidly changing areas in Antarctica. The large volume of
385 ice loss in this area causes large elastic loading responses. Groh et al. (2012) and Gunter et al.
386 (2013) have both mentioned the possibility of a present-day viscoelastic signal in this area. Our
387 uplift estimate for basin 21 is comparably small at 0.6mm/yr. AGE-1 (0.7 mm/yr) is closest to this
388 estimate, while IJ05 (1.6 mm/yr) and W12a (3.1 mm/yr) are considerably higher. Gunter13 has
389 the highest rate at 5.4mm/yr. In basin 22, again, we agree best with AGE-1 (1.1mm/yr, RATES at
390 0.9 mm/yr), while all other estimates are higher. Gunter and W12a cover the higher end at 4.5
391 mm/yr and 4.8 mm/yr respectively, and IJ05-R2 lies in the middle at 3.0 mm/yr. Basin 23, which
392 connects the ASE to the Southern Peninsula, also yields a small uplift rate (0.4mm/yr). AGE-1
393 (0.5mm/yr) lies within the error estimate, with IJ05-R2 (1.7mm/yr) and Gunter13 (2.0mm/yr) just
394 outside, and W12a considerably higher at 5 mm/yr.

395 On the Southern Peninsula (basin 24), agreement with AGE-1 (1.2 mm/yr, RATES 1.3 mm/yr) is
396 very good, but W12a is close (1.8 mm/yr). Gunter13 and IJ05 both show uplift on the Southern
397 Peninsula, but at a higher rate of 2.4 mm/yr and 3.1 mm/yr, respectively. On the Northern
398 Peninsula, again the agreement is best with AGE-1 (0.8 mm/yr, RATES 0.7 mm/yr), followed by
399 IJ05-R2 (0.5 mm/yr). The W12a rate is higher at 1.7 mm/yr. Gunter13 is the only model that
400 shows a negative GIA trend (-0.70 mm/yr) in this region.

401 5 Discussion

402 In Fig. 13 and Table 3 we present the basin-scale combined ice and SMB loss in comparison with
403 two recent studies using GRACE (King et al., 2012), Sasgen et al., 2013). The latter study spans
404 the ICESat period and the rates were derived for this publication. The former study, however,
405 spans the 2002–2010 period. Basin definitions are the same as those in Sasgen et al. (2013) (as
406 shown in Fig. 11) but differ from King et al. (2012): the sum of our basins 1 and 24 match the sum
407 of their basins 1, 24 and 27. Our basin 25 matches the sum of their basins 25 and 26.
408 Consequently, comparisons for these basins are not shown in Fig. 13 but provided in Table 3.

409 Overall, we obtain good agreement with Sasgen et al. (2013). Our mean, time-averaged ice loss
410 rate of -76 ± 15 GT/yr, deviates by less than one standard deviation from the value of -87 ± 10
411 GT/yr obtained by Sasgen et al. (2013). Agreement at the basin scale is also good. For Basin 18,
412 our error estimates are inflated because of the pole gap in the altimetry data. The largest
413 differences occur in basins 19, 20 and 23. For 19 and 20, agreement is very good when comparing
414 the sums of the two adjacent basins – suggesting that leakage effects might be affecting the ability
415 of a GRACE-only solution to fully isolate the signal to each basin. For basin 23, the altimetry –
416 both EnviSat and ICESat – show a clear positive trend in this area (ICESat: $+4$ GT/yr), with only
417 very localized ice loss signals on Ferrigno ice stream. This positive trend (as opposed to a
418 negative trend from GRACE) reduces the ice loss estimate and causes the difference between the
419 two estimates. The strong GRACE mass loss signal for the Amundsen Sea sector leads to
420 increased leakage in the coastal basins. The King et al. (2012) result shows basins 23 and 21 are
421 strongly correlated at $p=0.96$. When comparing the sum over the coastal basins 21, 22, and 23, the
422 difference between the Sasgen et al. (2013) estimate (-80 GT/yr) and ours (-74 GT/yr) reduces to
423 6 GT/yr.

424 We also compare our basin scale results to ice loss rates from King et al. (2012). Here, the
425 observation periods are not identical, and the GIA estimates differ. Still, there is generally good
426 agreement at the basin-scale, in particular, where their GIA estimates (Whitehouse et al., 2012) lie
427 within our error ranges (basins 18, 19) and worst where their GIA uplift rate is a multiple of ours
428 (sum of basins 1 and 24). Overall, their ice loss rate of -118 ± 9 GT/yr is significantly higher than
429 ours.

430 Integrated over the domain studied, our loss estimate is lower than other recent estimates:
431 Shepherd et al. (2012) arrive at -97 ± 20 Gt/yr for WAIS over the ICESat period; while Gunter et
432 al. (2013) obtain -105 ± 22 Gt/yr. With regards to Shepherd et al. (2012) and other altimetry-based
433 results, the discrepancy is partly explained by our estimate of a negative SMB anomaly in the
434 ASE, while RACMO2.1 gives a positive trend in this region (Fig. 5). Methodologies employing
435 RACMO2.1 will, thus, attribute a greater loss (for a given height change) to ice dynamics. Since
436 these losses occur at a higher density than SMB, the inferred mass loss is greater. With regards to
437 Gunter et al. (2013), the discrepancy arises from the different GIA rates used in the ASE. One
438 cause for this might be the different GRACE solutions used. Our GRACE data set (Luthcke et al.,
439 2013) is equivalent to a RL04 GRACE solution and uses the same antialiasing products. In Gunter
440 et al. (2013), RL05 GRACE solutions appear to yield higher overall mass loss estimates.

441 Preliminary comparisons of new (RL05) mascon solutions with the RL04 ones appear to show,
442 however, little impact on the trends.

443 The results for SMB are more challenging to interpret because the trend, over this time period, is
444 relatively small (a few cm/yr) and below one standard deviation for most of the domain (Fig 6).
445 There is, however, some agreement with new *in-situ* data from ice cores (Medley et al., 2013;
446 Burgener et al., 2013). It should be remarked that in the ASE, where we also observe an ice loss
447 maximum, the statistical framework might have difficulty in partitioning SMB and ice dynamics.
448 The reason for this is that the density of the SMB changes tends to be higher at the coast, with
449 higher temperatures and melt rates. Some of the large, negative trends seen in the ASE could thus
450 be falsely attributed to SMB. This could be remedied in principle by including more information
451 on the spatial patterns of SMB into our framework by using, for example, a more informative
452 prior. Also, it should be noted that the uncertainties on our SMB rates, although low on a basin
453 scale, are comparatively high on a small spatial scale. These issues will become less critical in a
454 time-evolving solution because ice dynamics and SMB have very different temporal frequencies:
455 the former tends to vary smoothly in time, while the latter has relatively large high-frequency
456 variability. This important difference in temporal smoothness will elicit significant improvement
457 in source separation.

458 Methods that combine altimetry and gravimetry such as Gunter et al. (2013) and also the
459 framework presented here are sensitive to the SMB anomaly used. We illustrate this sensitivity
460 through a simple calculation: let the unobserved processes on a 1 m^2 unit area be as follows: SMB
461 amounts to 0.2 m/yr at 350 kg/m^3 density; GIA is 1 mm/yr at 3500 kg/m^3 ; and ice loss is at -1.0
462 m/yr at 917 kg/m^3 . This amounts to an observed height change of -0.799 m/yr . The observed mass
463 change is -897.5 kg/yr over the unit area. We now try to explain these signals by taking into
464 account GRACE and altimetry, but erroneously assume a SMB rate that is 10% too high at
465 0.22 m/yr (amounting to a positive mass change of 77 kg/yr). The remaining mass signal that
466 needs to be explained by ice and GIA is now -974.5 kg/yr . The unexplained height change is $-$
467 1.019 m . We arrive at two equations, one for height and one for mass, that can be solved by
468 finding the intersection of the two lines (see Fig. 14). Solving the equations, we arrive at an ice
469 mass loss rate of -1.025 m/yr with a high, but still plausible, GIA rate of 6 mm/yr . Thus, in this
470 example, a 10% difference in SMB can result in a GIA estimate that is markedly higher (5 mm/yr)
471 than the truth. The resulting ice mass difference would be in the range of -40 Gt/yr when taken
472 over the whole of West Antarctica. Naturally, this sensitivity acts both ways, so an underestimate
473 in SMB would result in a lower GIA, and less ice loss. In this context, both GRACE filtering and
474 the treatment of the ICESat trends also play a major rôle. As the mass loss signal in West
475 Antarctica is highly localised, with high rates of elevation change confined to only a few percent
476 of the area of a basin, the inclusion or exclusion of a single (informative) altimetry data point can
477 alter the spatial distribution of height change considerably but less, the overall mass trend, as this
478 is constrained by GRACE.

479 It is also worth examining the sensitivity of the solution to the prior distributions that were derived
480 from the forward models, auxiliary data sets, such as surface ice velocity, and expert knowledge.
481 To do this, we changed the original amplitude and length-scale constraints as detailed in Table 4.
482 The Table also lists the original mass trend (using constraints detailed in Table 2) alongside the

483 new estimates using the revised constraints. Changes in the characteristic length scale for GIA
484 and SMB have a rather small effect on the integrated mass trend. On the other hand, the velocity
485 threshold that is used to determine whether the signal is likely to be associated with ice dynamics
486 appears to have a significant effect for the three basins that comprise the Antarctic Peninsula: 23,
487 24, 25. This is because, for the Peninsula, observed and balance velocities are missing in a number
488 of places. Where this is the case, they were set to 5 m/yr. With a 50 m/yr soft threshold this means
489 that an ice dynamics signal is extremely unlikely in all locations with a missing velocity.
490 Improving the velocity field in this area would, therefore, reduce this sensitivity.

491 The GIA estimates from our study agree well with a recent GRACE-based estimate (Sasgen et al.,
492 2013) and also compare well with a recent forward model (Ivins et al., 2013). Compared to AGE-
493 1, the spatial pattern of our uplift maximum is shifted away from the Peninsula and towards the
494 Ronne Ice Shelf. The spatial pattern is closer to that of W12a and ICE-5G models, with a bimodal
495 uplift maximum centred underneath the Ronne and Ross Ice Shelves (Fig 9). This spatial structure
496 is likely to have resulted from the use of GPS uplift rates, which were also used in the calibration
497 of the most recent forward models (Whitehouse et al., 2012), Ivins et al., 2013). The W12a model
498 yields slightly higher estimates for most basins but shows good agreement on the Southern
499 Antarctic Peninsula. Whitehouse et al. (2012) remark that the uplift rates using the W12 de-
500 glaciation history – which are already substantially lower than the ICE-5G (Peltier 2004) model
501 rates – can be viewed as an upper bound. Separating secular and present-day viscous and elastic
502 signals from the trends in this area remains a challenging task and will be treated in greater detail
503 in the spatio-temporal version of our framework.

504 For this proof-of-concept study, our focus lies mainly on ice dynamics, SMB and GIA estimates,
505 neglecting to a certain extent the influence of mass-invariant height changes (due to firn
506 compaction and elastic uplift of the bedrock). At this stage, the framework solves for a single
507 process that combines elastic rebound and firn compaction. In this time-invariant framework, the
508 two are confounded and cannot be separated, as they are not distinguishable by different densities
509 or length scales. A better approach to solve for the elastic rebound of the crust would be to
510 integrate a dynamic estimate that depends on the ice load changes. This approach is being
511 implemented in the spatiotemporal version of the framework. Firn compaction is currently linked
512 with SMB through a simple correlation model (Zammit-Mangion et al., 2014). This approach
513 could be further improved by adding a temperature dependence, following the principles of a
514 simple firn compaction model (Helsen et al., 2008). Finally, another open question concerns the
515 extent of present-day viscoelastic rebound in the ASE..

516 **6 Conclusion**

517 Our proof-of-concept study shows that hierarchical modelling is a powerful tool in separating ice
518 mass balance, SMB and GIA processes when combining satellite altimetry, GPS and gravimetry.
519 We demonstrate that, using only smoothness criteria derived from forward models, it can provide
520 an accurate estimate of the different processes. A time-varying version of the framework is
521 currently being developed, which includes a number of improvements, mentioned earlier. In
522 particular, estimation of elastic rebound in the GPS time series, and more robust partitioning of
523 ice dynamics and SMB will provide substantial improvements in source separation, error

524 reduction and GIA estimation. A central advantage of the framework is that new data – which
525 need be neither regular, or gridded – can be added at any point. For example, it is possible to
526 extend the observation period forward or back in time using data from ERS2, or Cryosat2, or any
527 other data set that contains information about one of the processes being solved for. This could
528 include, for example, accumulation radar data or shallow ice cores for SMB variability or
529 additional GPS sites as they become available. Preliminary tests have shown that the inference can
530 also be performed without GRACE data. .

531 **Acknowledgements**

532 The authors would like to thank the following colleagues for helpful discussions: Volker
533 Klemann, Ingo Sasgen, Matt King, Liz Petrie, Pete Clarke, Martin Horwath, Finn Lindgren and
534 Valentina Barletta. This work was funded by UK NERC grant NE/I027401/1.

535 Also, the following colleagues provided additional data without which the project would not have
536 been possible: J.M. Lenaerts, S. Ligtenberg, Erik Ivins, Ricardo Riva, Brian Gunter, Pippa
537 Whitehouse, Ingo Sasgen, Rory Bingham, Grace Nield, Liz Thomas.

538 **References**

539 Arthern, R. J., Vaughan, D. G., Rankin, A. M., Mulvaney, R., and Thomas, E. R.: In situ
540 measurements of Antarctic snow compaction compared with predictions of models, *Journal of*
541 *Geophysical Research*, 115, 2010, 10.1029/2009jf001306.

542 Bamber, J. L., Vaughan, D. G., & Joughin, I.: Widespread complex flow in the interior of the
543 Antarctic ice sheet. *Science*, 287(5456), 1248-1250, 2000.

544 Bamber, J. L., Gomez-Dans, J. L., & Griggs, J. A.: A new 1 km digital elevation model of the
545 Antarctic derived from combined satellite radar and laser data–Part 1: Data and methods. *The*
546 *Cryosphere*, 3(1), 101-111, 2009.

547 Barletta, V. R., Sørensen, L. S., & Forsberg, R.: Variability of mass changes at basin scale for
548 Greenland and Antarctica. *The Cryosphere Discussions*, 6(4), 3397-3446, 2012.

549 Berthier, E., Scambos, T. A., & Shuman, C. A.: Mass loss of Larsen B tributary glaciers
550 (Antarctic Peninsula) unabated since 2002. *Geophysical Research Letters*, 39, L13501,
551 doi:10.1029/2012GL051755 , 2012.

552 Borsa, A. A., Moholdt, G., Fricker, H. A., and Brunt, K. M.: A range correction for ICESat and its
553 potential impact on ice-sheet mass balance studies, *The Cryosphere*, 8, 345-357, 2014.

554
555 Burgener, L., et al.: An observed negative trend in West Antarctic accumulation rates from 1975
556 to 2010: evidence from new observed and simulated records. *Journal of Geophysical Research:*
557 *Atmospheres*, 118, 1–12, doi:10.1002/jgrd.50362, 2013.

558 Chen, J. L., et al.: "Antarctic mass rates from GRACE." *Geophysical Research Letters*, 33,
559 L11502, 2006.

- 560 Davis, C. H.: Temporal change in the extinction coefficient of snow on the Greenland ice sheet
561 from an analysis of seasat and geosat altimeter data, *IEEE Trans. Geosci. Remote Sensing*, 34,
562 1066-1073, 1996.
- 563 De Angelis, H. and Skvarca, P.: Glacier surge after ice shelf collapse, *Science*, 299, 1560-1562,
564 2003.
565
- 566 Dee, D. P., et al.: The ERA-Interim reanalysis: Configuration and performance of the data
567 assimilation system. *Quarterly Journal of the Royal Meteorological Society* 137.656: 553-597,
568 2011.
- 569 Danesi, S., and Morelli, A.: Structure of the upper mantle under the Antarctic Plate from surface
570 wave tomography. *Geophysical Research Letters* 28.23: 4395-4398, 2001.
- 571 Dobslaw, H., and Thomas, M.: Simulation and observation of global ocean mass anomalies.
572 *Journal of Geophysical Research: Oceans* (1978–2012), 112(C5), 2007.
- 573 Dobslaw, H., Flechtner, F., Bergmann-Wolf, I., Dahle, C., Dill, R., Esselborn, S., and Thomas,
574 M.: Simulating high-frequency atmosphere-ocean mass variability for dealiasing of satellite
575 gravity observations: AOD1B RL05. *Journal of Geophysical Research: Oceans*, 118(7), 3704-
576 3711, 2013.
- 577 Flament, T., & Rémy, F.: Dynamic thinning of Antarctic glaciers from along-track repeat radar
578 altimetry. *Journal of Glaciology*, 58(211), 830-840, 2012.
- 579 Fretwell, P. et al.: Bedmap2: improved ice bed, surface and thickness datasets for Antarctica. *The*
580 *Cryosphere*, 7(1), 375–393, 2013.
- 581 Frezzotti, M., Scarchilli, C., Becagli, S., Proposito, M., & Urbini, S.: A synthesis of the Antarctic
582 surface mass balance during the last 800 yr. *The Cryosphere*, 7(1), 303-319, 2013.
- 583 Groh, A., Ewert, H., Scheinert, M., Fritsche, M., Rülke, A., Richter, A., and Dietrich, R.: An
584 investigation of glacial isostatic adjustment over the Amundsen Sea Sector, West Antarctica.
585 *Global and Planetary Change*, 98, 45-53. 2012.
- 586 Gunter, B. C., et al.: Empirical estimation of present-day Antarctic glacial isostatic adjustment and
587 ice mass change. *The Cryosphere Discuss.*, 7, 3497-3541, 2013.
- 588 Helsen, M. M., van den Broeke, M. R., van de Wal, R. S., van de Berg, W. J., van Meijgaard, E.,
589 Davis, C. H., Goodwin, I.: Elevation changes in Antarctica mainly determined by accumulation
590 variability. *Science*, 320(5883), 1626-1629, 2008.
- 591 Hofton, M. A., Luthcke, S. B., & Blair, J. B.: Estimation of ICESat intercampaign elevation biases
592 from comparison of lidar data in East Antarctica. *Geophysical Research Letters*, 40(21), 5698-
593 5703, 2013.
- 594 Horwath, M. and Dietrich, R.: Signal and error in mass change inferences from GRACE: the case
595 of Antarctica, *Geophysical Journal International*, 177, 849-864, 2009.

- 596 Hurkmans, R. T. W. L., Bamber, J. L., Davis, C. H., Joughin, I. R., Khvorostovsky, K. S., Smith,
597 B. S., and Schoen, N.: Time-evolving mass loss of the Greenland Ice Sheet from satellite
598 altimetry, *The Cryosphere*, 8, 1725-1740, 2014.
- 599 Ivins, E. R., & James, T. S.: Antarctic glacial isostatic adjustment: a new assessment. *Antarctic*
600 *Science*, 17(04), 541-553, 2005.
- 601 Ivins, E. R., James, T. S., Wahr, J., Schrama, O., Ernst, J., Landerer, F. W., & Simon, K. M.:
602 Antarctic contribution to sea level rise observed by GRACE with improved GIA correction.
603 *Journal of Geophysical Research: Solid Earth*, 118(6), 3126-3141, 2013.
- 604 Karato, S.: Deformation of earth materials: an introduction to the rheology of solid earth.
605 Cambridge University Press, 2008.
- 606 King, M. A., Bingham, R. J., Moore, P., Whitehouse, P. L., Bentley, M. J., & Milne, G. A.: Lower
607 satellite-gravimetry estimates of Antarctic sea-level contribution. *Nature*, 491(7425), 586-589,
608 2012.
- 609 Kunz, M., King, M. A., Mills, J. P., Miller, P. E., Fox, A. J., Vaughan, D. G., & Marsh, S. H.:
610 Multi-decadal glacier surface lowering in the Antarctic Peninsula. *Geophysical Research Letters*,
611 39(19), L19502, doi:10.1029/2012GL052823, 2012.
- 612 Kusche, J., Schmidt, R., Petrovic, S., & Rietbroek, R.: Decorrelated GRACE time-variable gravity
613 solutions by GFZ, and their validation using a hydrological model. *Journal of Geodesy*, 83(10),
614 903-913, 2009.
- 615 Lenaerts, J. T. M., den Broeke, M. R., Berg, W. J., Meijgaard, E. V., & Kuipers Munneke, P.: A
616 new, high-resolution surface mass balance map of Antarctica (1979–2010) based on regional
617 atmospheric climate modeling. *Geophysical Research Letters*, 39(4), L04501, 2012.
- 618 Ligtenberg, S. R. M., Helsen, M. M., and van den Broeke, M. R.: An improved semi-empirical
619 model for the densification of Antarctic firn, *Cryosphere*, 5, 809-819, 2011.
- 620 Lindgren, F., Rue, H., & Lindström, J.: An explicit link between Gaussian fields and Gaussian
621 Markov random fields: the stochastic partial differential equation approach. *Journal of the Royal*
622 *Statistical Society: Series B (Statistical Methodology)*, 73(4), 423-498, 2011.
- 623 Luthcke, S. B., Arendt, A. A., Rowlands, D. D., McCarthy, J. J., and Larsen, C. F.: Recent glacier
624 mass changes in the Gulf of Alaska region from GRACE mascon solutions, *J. Glaciol.*, 54, 767-
625 777, 2008.
626
- 627 Luthcke, S. B., et al.: Antarctica, Greenland and Gulf of Alaska land-ice evolution from an
628 iterated GRACE global mascon solution. *Journal of Glaciology*, 59.216, 613-631, 2013.
- 629 Medley, B., et al.: Airborne-radar and ice-core observations of annual snow accumulation over
630 Thwaites Glacier, West Antarctica confirm the spatiotemporal variability of global and regional
631 atmospheric models. *Geophysical Research Letters* 40.14: 3649-3654, 2013.

632 Moholdt, G., Nuth, C., Hagen, J. O., & Kohler, J.: Recent elevation changes of Svalbard glaciers
633 derived from ICESat laser altimetry. *Remote Sensing of Environment*, 114(11), 2756-2767, 2010.

634 Osmanoglu, B., Braun, M., Hock, R., & Navarro, F. J.: Surface velocity and ice discharge of the
635 ice cap on King George Island, Antarctica. *Annals of Glaciology*, 54(63), 111-119, 2013.

636 Peltier, W. R.: Global glacial isostasy and the surface of the ice-age Earth: The ICE-5G (VM2)
637 model and GRACE. *Annu. Rev. Earth Planet. Sci.*, 32, 111-149., 2004.

638 Retzlaff, R., & Bentley, C. R.: Timing of stagnation of Ice Stream C, West Antarctica, from short-
639 pulse radar studies of buried surface crevasses. *Journal of Glaciology*, 39(133), 1993.

640 Rignot, E., Velicogna, I., Van den Broeke, M. R., Monaghan, A., & Lenaerts, J. T. M.:
641 Acceleration of the contribution of the Greenland and Antarctic ice sheets to sea level rise.
642 *Geophysical Research Letters*, 38(5), L05503, 2011.

643 Sasgen, I., Martinec, Z., & Bamber, J.: Combined GRACE and InSAR estimate of West Antarctic
644 ice mass loss. *Journal of Geophysical Research: Earth Surface* (2003–2012), 115(F4), 2010.

645 Sasgen, I., et al.: Antarctic ice-mass balance 2003 to 2012: regional reanalysis of GRACE satellite
646 gravimetry measurements with improved estimate of glacial-isostatic adjustment based on GPS
647 uplift rates. *The Cryosphere Discuss.*, 6, 3703-3732, 2012.

648 Scambos, T. A., Bohlander, J. A., Shuman, C. U., & Skvarca, P.: Glacier acceleration and
649 thinning after ice shelf collapse in the Larsen B embayment, Antarctica. *Geophysical Research*
650 *Letters*, 31(18), L18402, 2004.

651 Shepherd, A. et al.: A reconciled estimate of ice-sheet mass balance. *Science*, 338(6111), 1183-
652 1189, 2012.

653 Sørensen, Louise Sandberg, et al.: Mass balance of the Greenland ice sheet (2003–2008) from
654 ICESat data - the impact of interpolation, sampling and firn density. *The Cryosphere*, 5, 173-186,
655 2011.

656 Swenson, S., Chambers, D., & Wahr, J.: Estimating geocenter variations from a combination of
657 GRACE and ocean model output. *Journal of Geophysical Research: Solid Earth* (1978–2012),
658 113(B8), 2008.

659 Tapley, B. D., Bettadpur, S., Ries, J. C., Thompson, P. F., & Watkins, M. M.: GRACE
660 measurements of mass variability in the Earth system. *Science*, 305(5683), 503-505, 2004.

661 Van de Berg, W. J., van den Broeke, M. R., van Meijgaard, E., and Reijmer, C. H.: Reassessment
662 of the Antarctic surface mass balance using calibrated output of a regional atmospheric climate
663 model, *J Geophys Res*, 111, D11104, doi:10.1029/2005JD006495, 2006.

664 Velicogna, I., & Wahr, J.: Measurements of time-variable gravity show mass loss in Antarctica.
665 *science*, 311(5768), 1754-1756, 2006.

666 Werth, S., Güntner, A., Schmidt, R., & Kusche, J.: Evaluation of GRACE filter tools from a
667 hydrological perspective. *Geophysical Journal International*, 179(3), 1499-1515, 2009.

668 Whitehouse, P. L., Bentley, M. J., Milne, G. A., King, M. A., & Thomas, I. D.: A new glacial
669 isostatic adjustment model for Antarctica: calibrated and tested using observations of relative sea-
670 level change and present ~~day uplift rates on Greenland~~ *Journal of Glaciology*, 54-1482,
671 2012.

672 Wouters, B., Chambers, D., & Schrama, E. J. O.: GRACE observes small-scale mass loss in
673 Greenland. *Geophysical Research Letters*, 35(20), L20501, 2008.

674 Yan, X. *Linear regression analysis: theory and computing*. World Scientific, 2009.

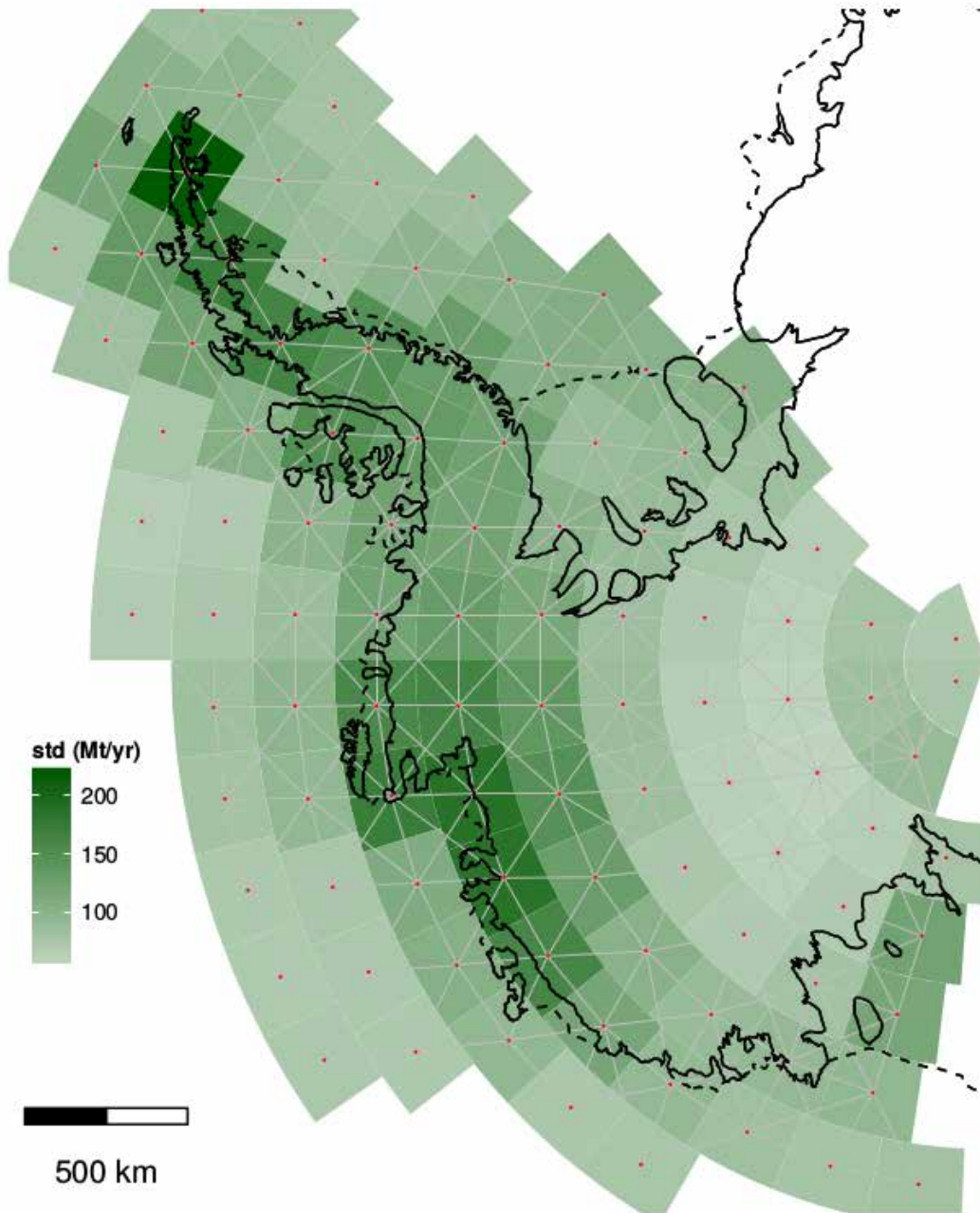
675 Zammit-Mangion, A., Rougier, J., Bamber, J., and Schön, N.: Resolving the Antarctic
676 contribution to sea-level rise: a hierarchical modelling framework, *Environmetrics*, 25, 245-264,
677 2014..

678 Zammit-Mangion, A., Bamber, J. L., Schoen, N. W., and Rougier, J. C.: A data-driven approach
679 for assessing ice-sheet mass balance in space and time, *Annals of Glaciology*, 56, XXX, 2015.

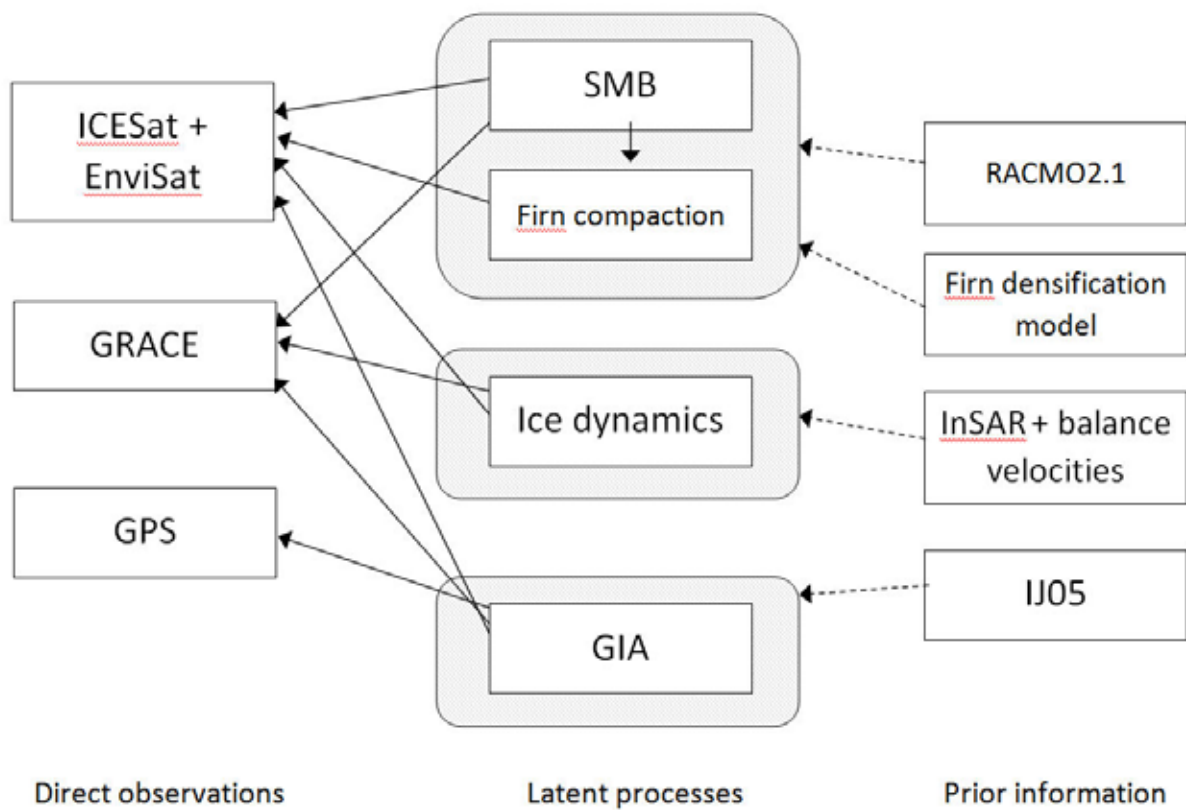
680 Zwally, H. J., and Brenner, A. C.: Ice sheet dynamics and mass balance. *International*
681 *Geophysics*, 69, 351-xxvi, 2001.

682 Zwally, H. et al.: *GLAS/ICESat L2 Antarctic and Greenland Ice Sheet Altimetry Data. Version*
683 *33*. Boulder, Colorado USA: National Snow and Ice Data Center, 2011.

684
685
686
687
688
689



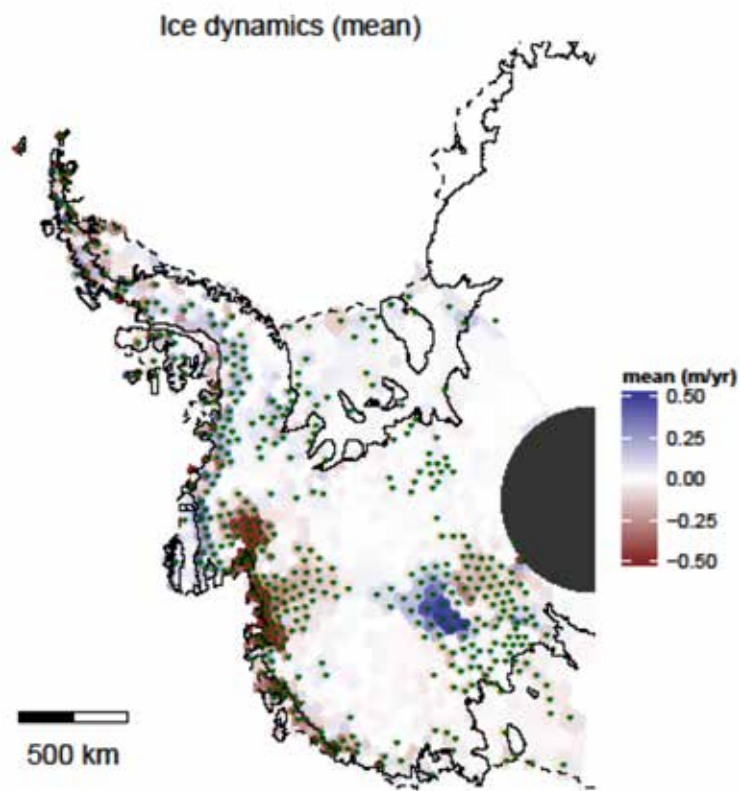
690
691 Figure 1. Error estimates for the GRACE mascon solutions, derived from a regression of the data
692 (Zammit-Mangion, et al, 2014).
693



694

695

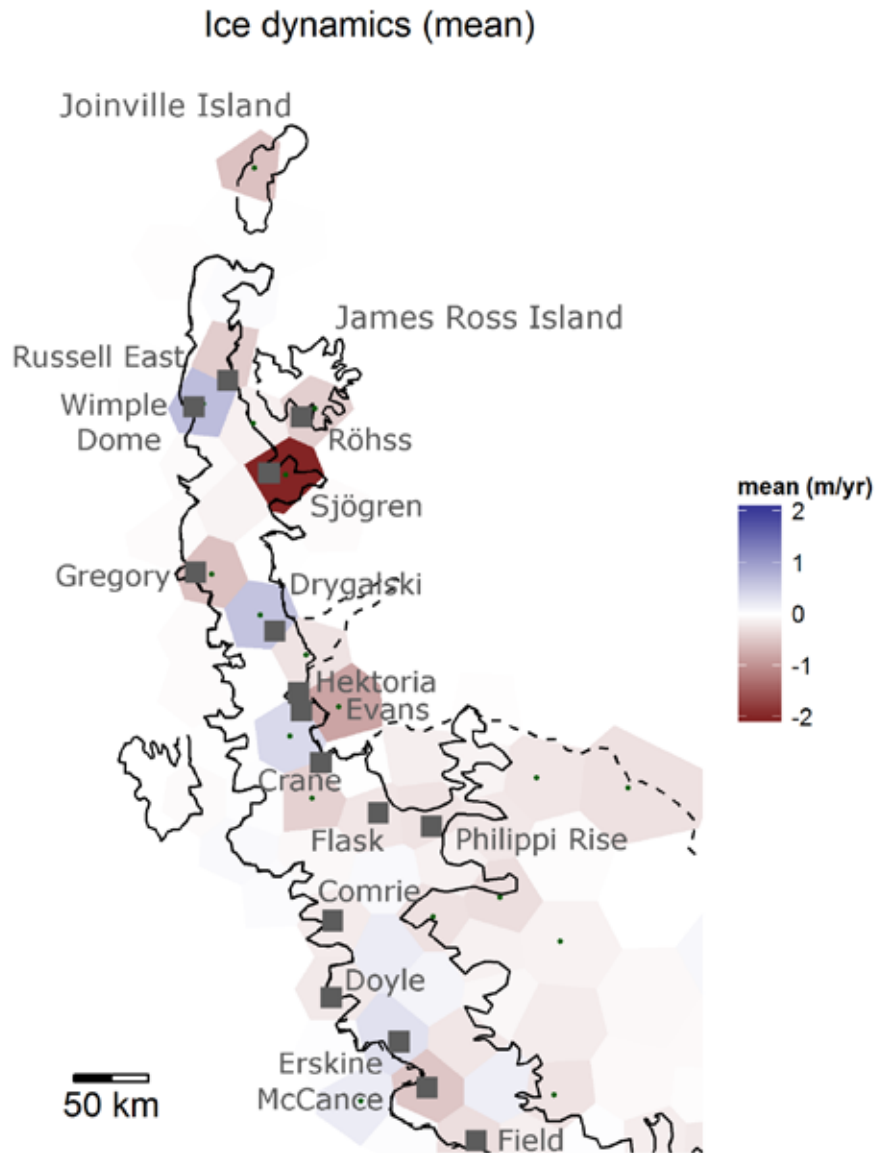
696 Figure 2. Schematic diagram showing the relationship between the observations, process model
 697 defining the latent processes and the priors employed.



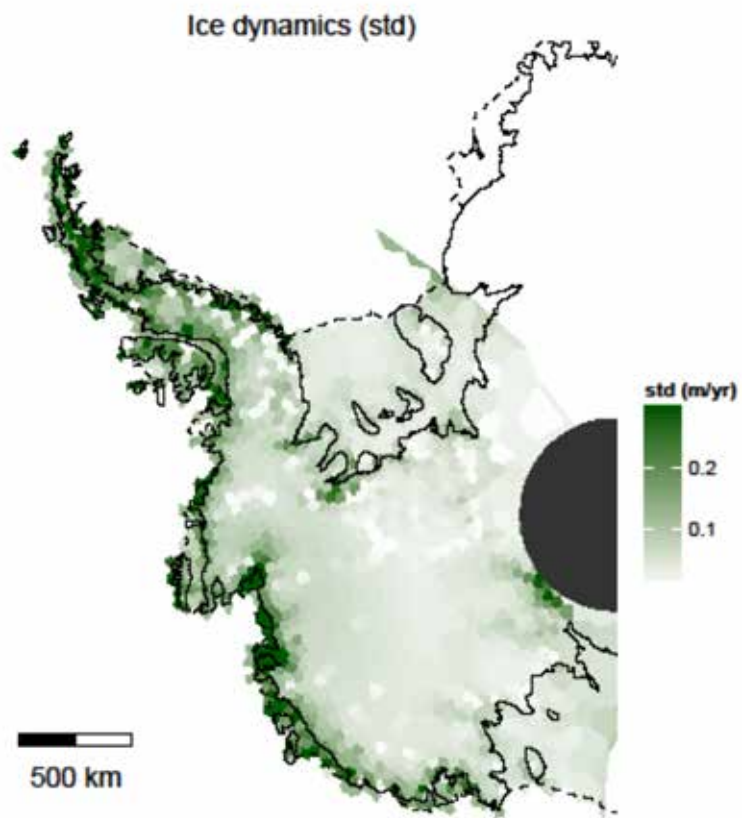
698

699

700 Figure 3a. Ice dynamics for 2003–2009 in m/yr. Stippled points denote areas in which the mean
701 signal is larger than the marginal standard deviation.



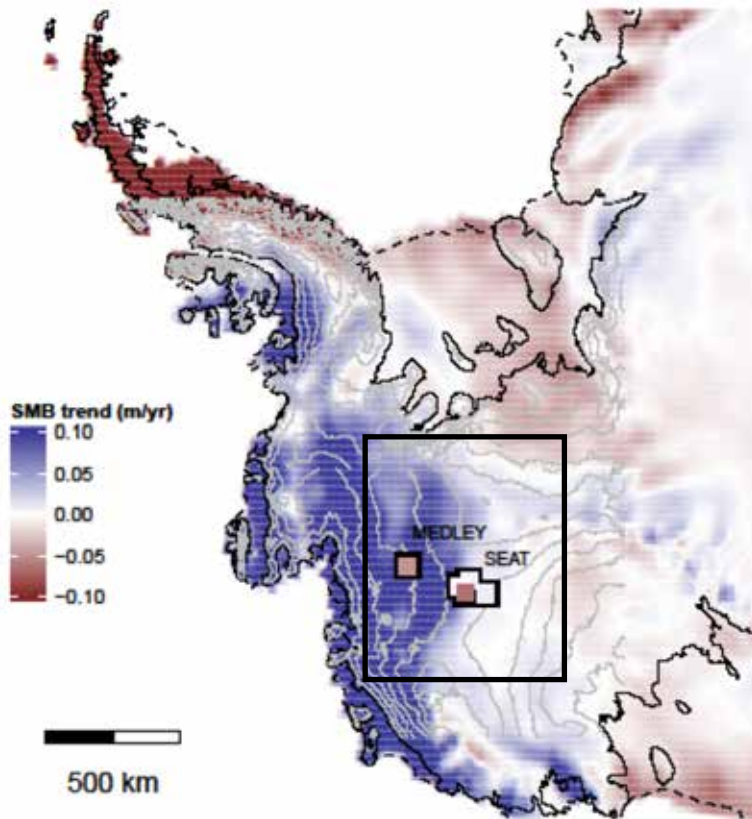
702
 703 Figure 3b. Ice dynamics for 2003–2009 in m/yr. Close-up for the Northern Antarctic Peninsula,
 704 with glacier locations (grey squares).
 705
 706



707

708 Figure 4. Marginal standard deviation of ice dynamics for 2003–2009 in m/yr.

RACMO trend of cumulative SMB anomalies 2003–2009



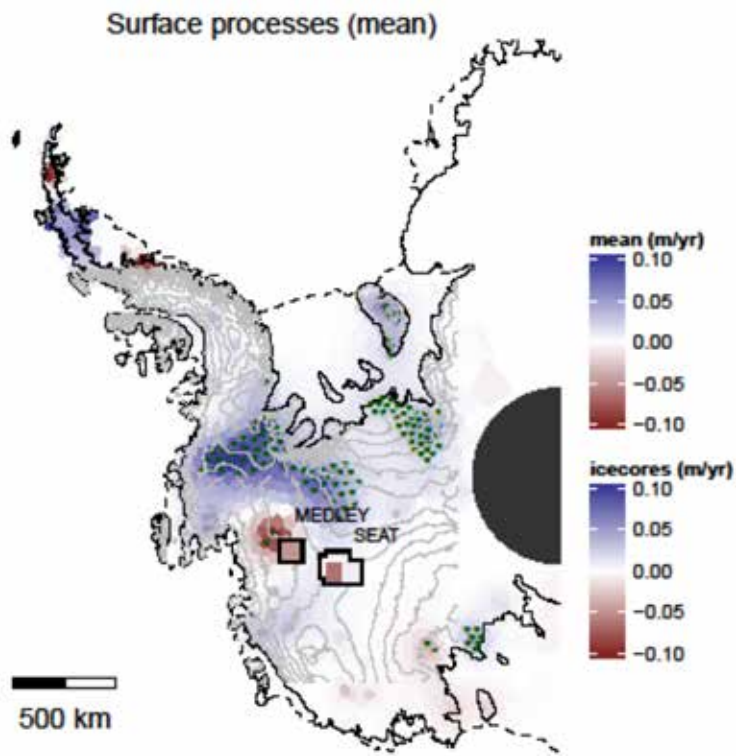
709

710

711

Figure 5. The SMB trend for 2003–2009 as obtained from RACMO. Contour lines (shown from -
1000 to 10000m Northing) are elevations from BEDMAP surface (Fretwell et al., 2013). Mean ice
core accumulation rates from Medley et al. (2013) (denoted MEDLEY) and ice core accumulation
rates from Burgener et al. (2013) (denoted SEAT). Rectangle shows area in close-up (Fig. 5).

715

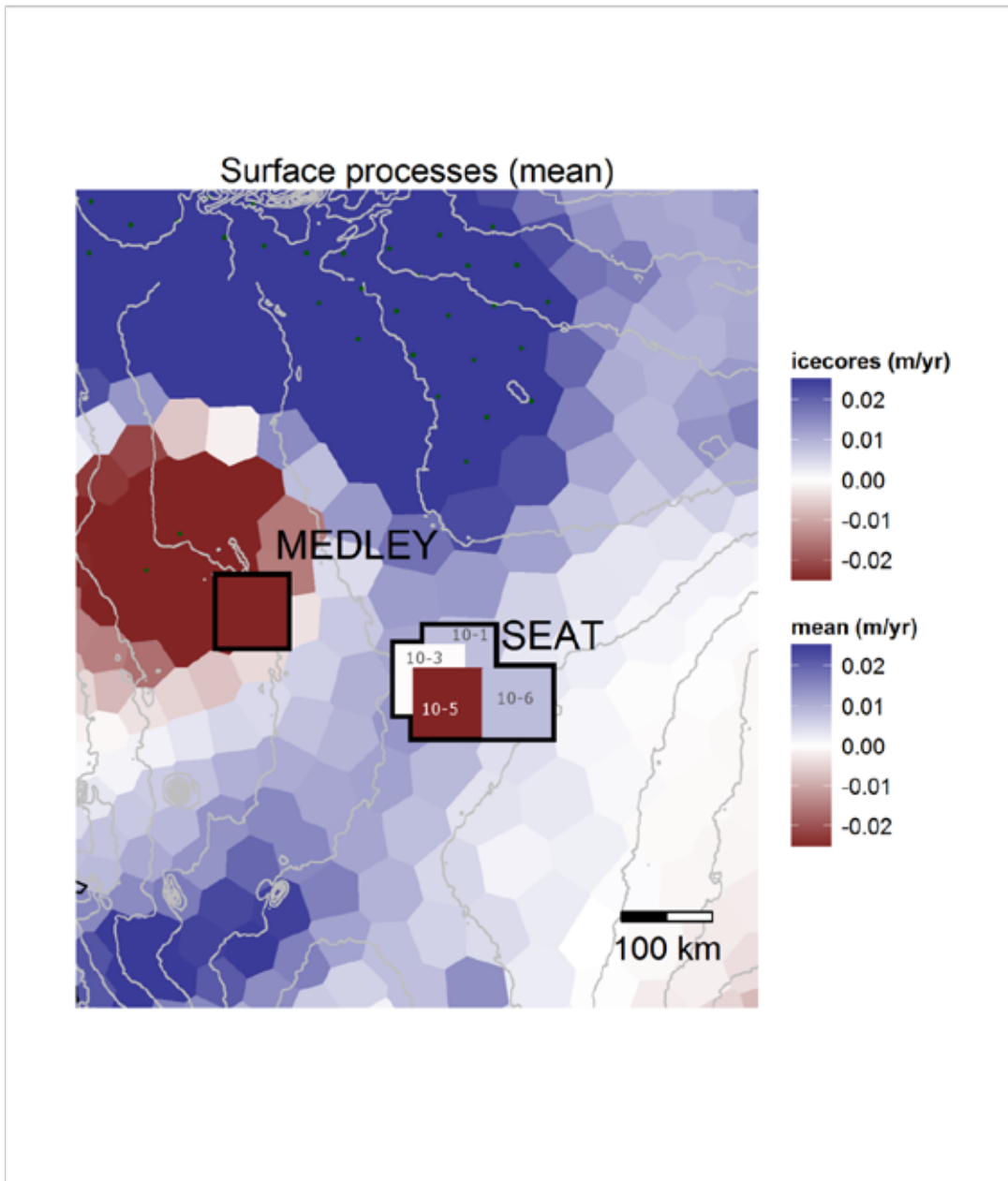


716

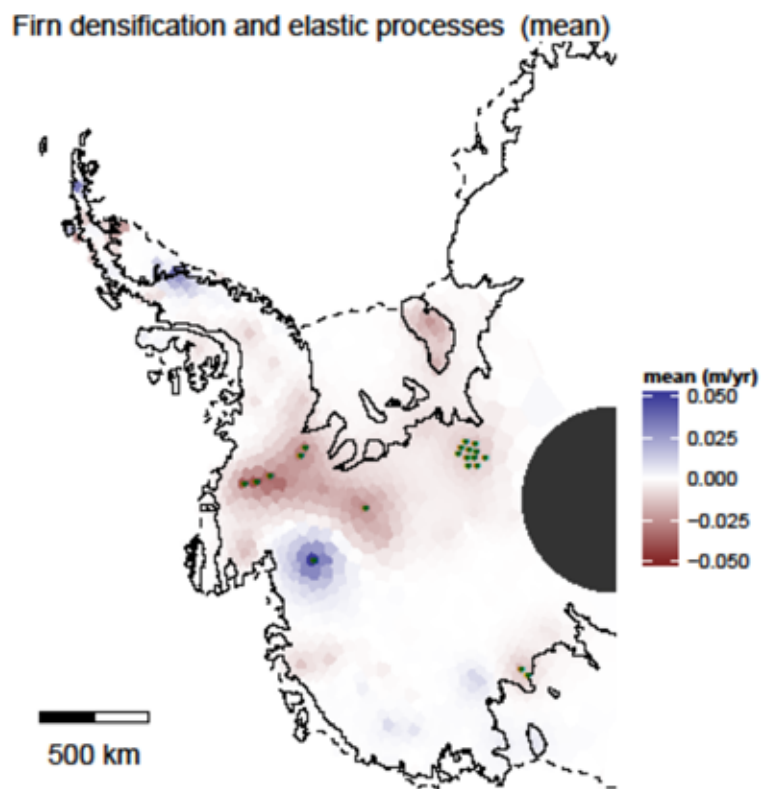
717

718

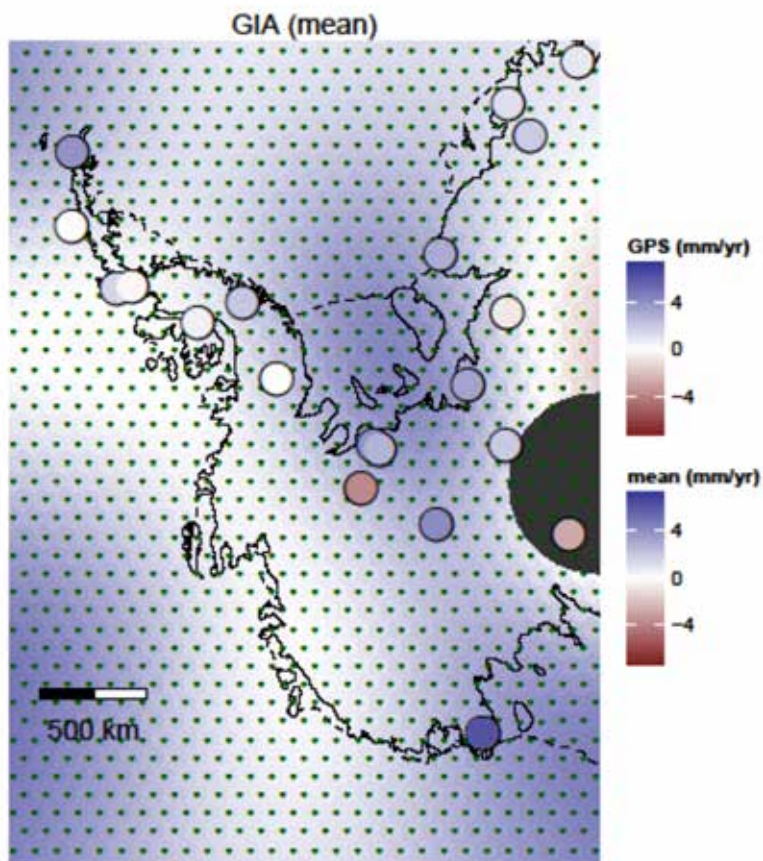
719 Figure 6. SMB rates for 2003–2009 in m/yr and locations of the ice cores from Burgener et al.
 720 (2013) and Medley et al. (2013). Contour lines are elevations from the BEDMAP surface
 721 (Fretwell et al., 2013). Stippled points denote areas in which the mean signal is larger than the
 722 marginal standard deviation.



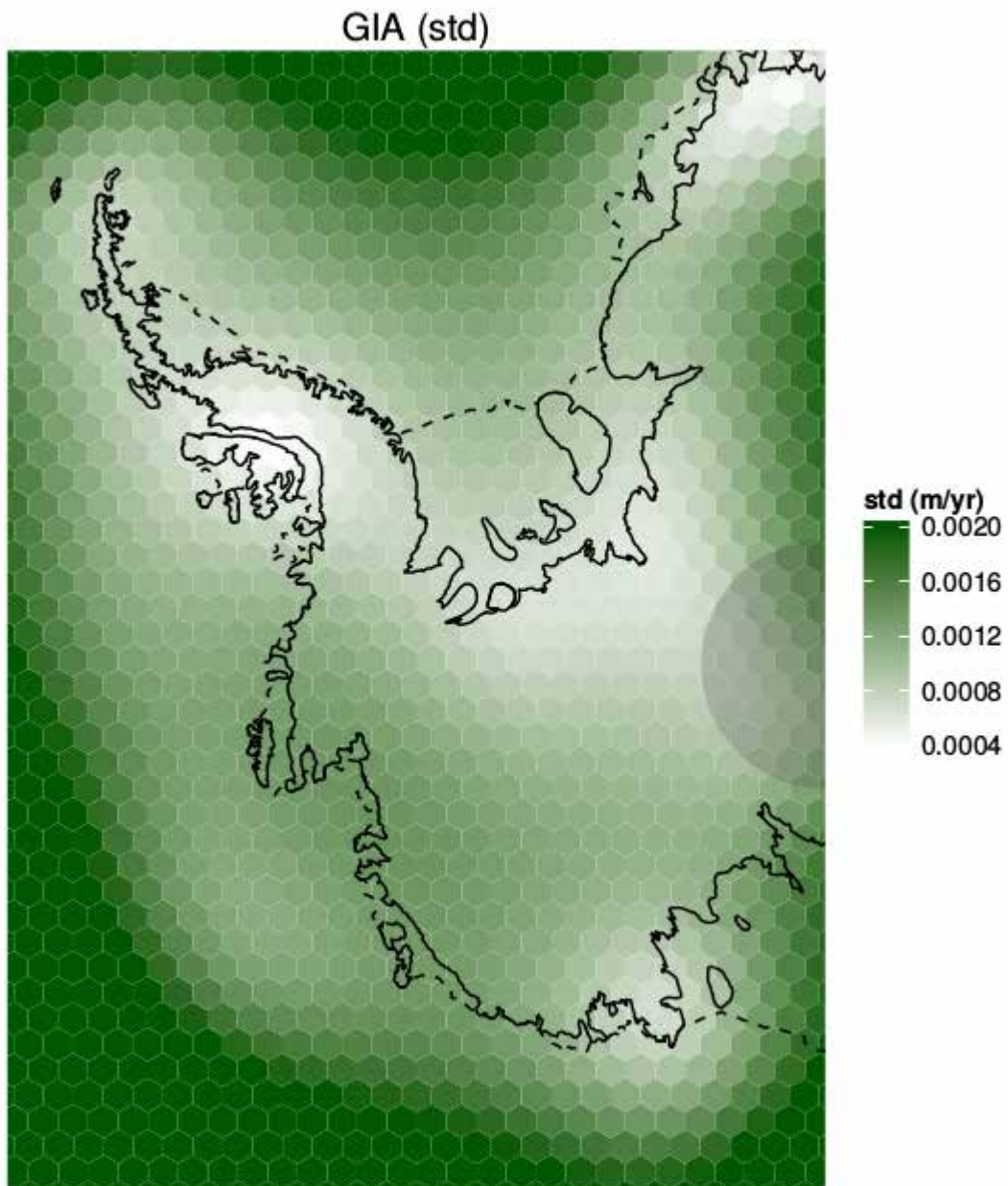
723
 724 Figure 7. Close-up of ice core mean from Medley et al. (2013) (denoted MEDLEY) and ice cores
 725 from Burgener et al. and RATES SMB trends for 2003–2009 in the Amundsen Sea Embayment.
 726 Numbers denote SEAT ice cores 10-1, 10-3, 10-5, and 10-6. Contour lines are elevations from
 727 BEDMAP surface (Fretwell et al., 2013). Stippled points denote areas in which the mean signal is
 728 larger than the marginal standard deviation.



729
 730 Figure 8. Height changes from firn compaction and elastic uplift of the crust for 2003–2009 in
 731 m/yr. Stippled points denote areas in which the mean signal is larger than the marginal standard
 732 deviation.
 733



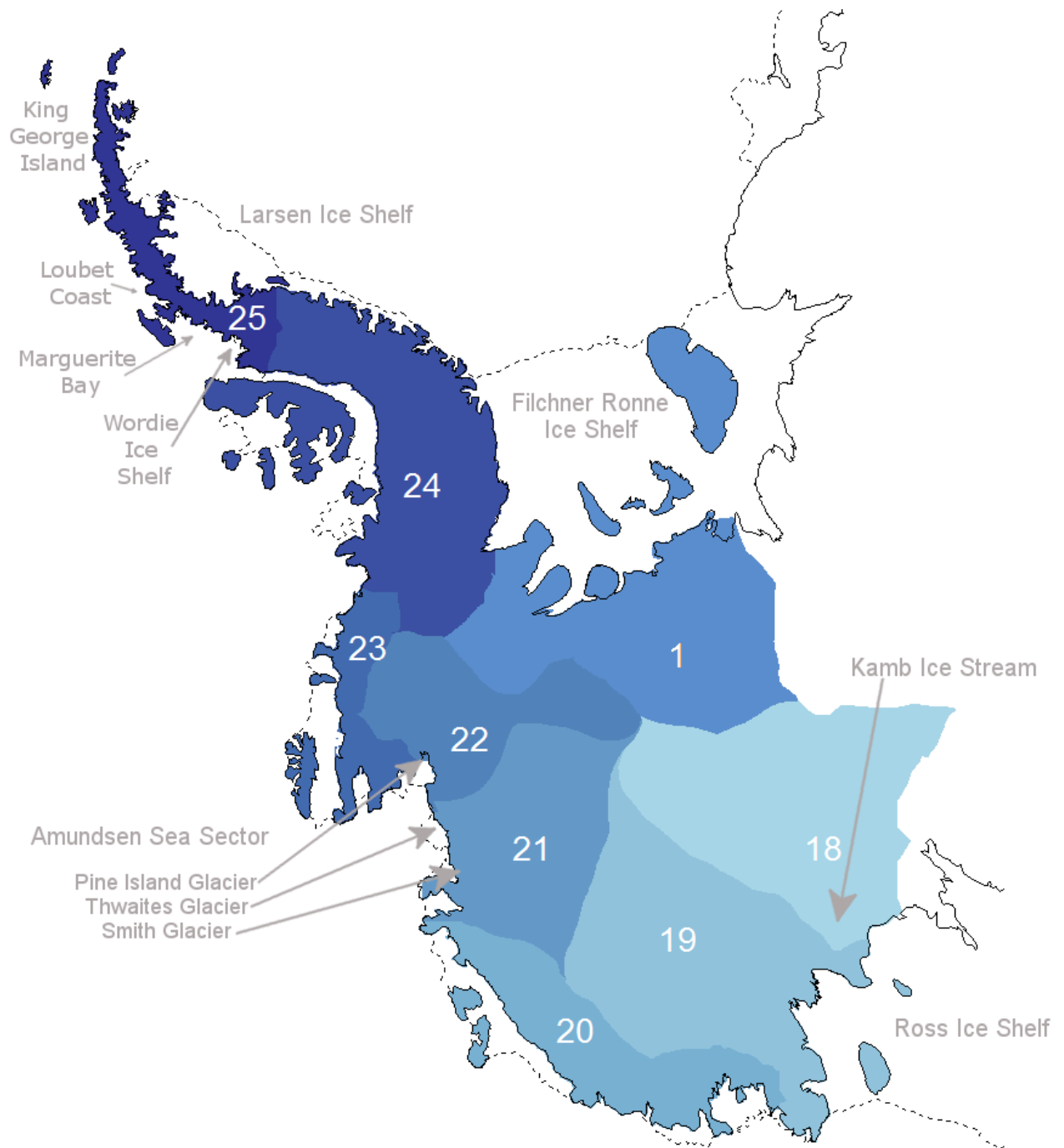
734
 735 Figure 9. GIA estimate with GPS stations and their rates. Stippled points denote areas in which
 736 the mean signal is larger than the marginal standard deviation.
 737



738

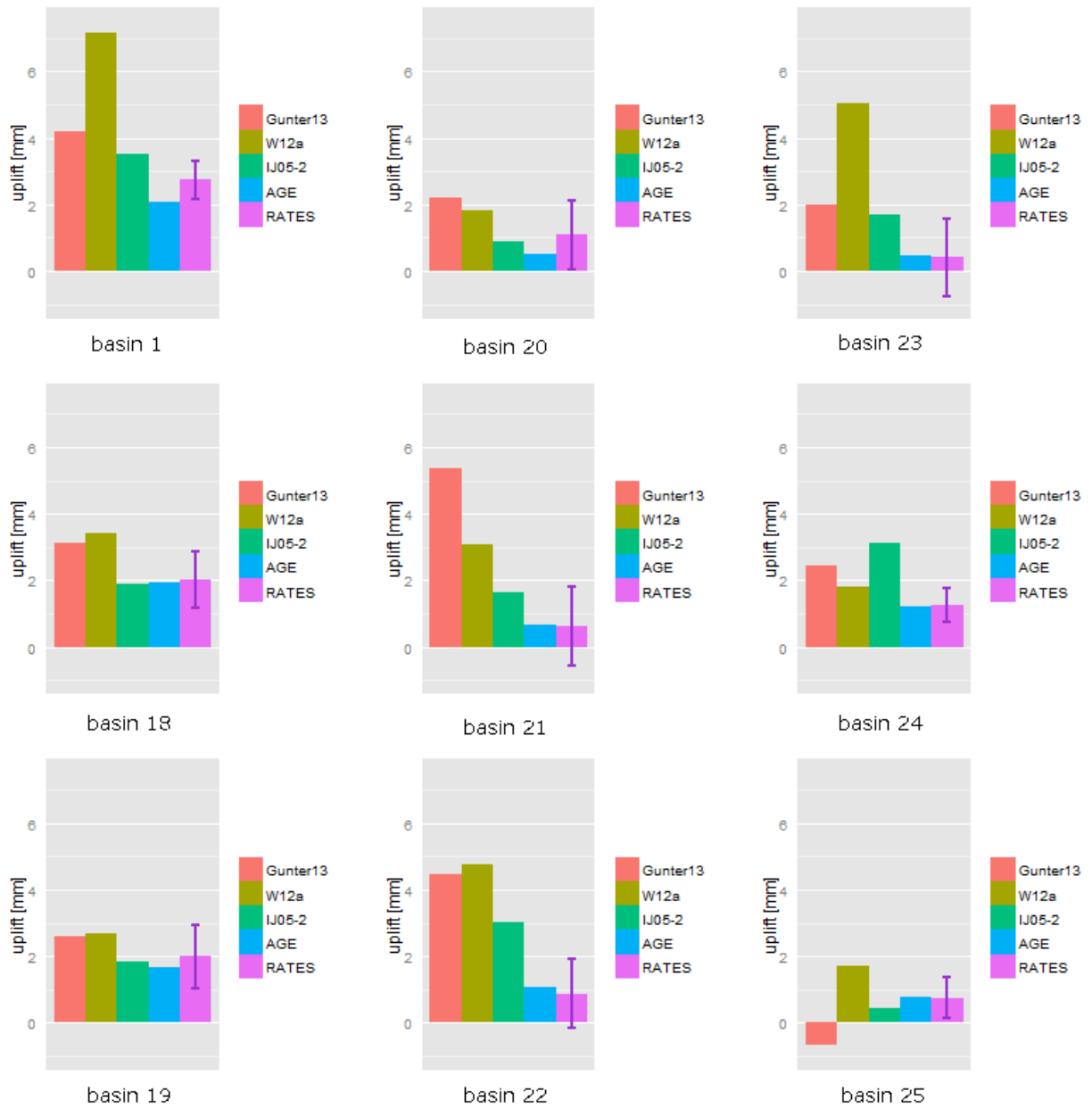
739 Figure 10. GIA error estimate (one standard deviation).

740



741

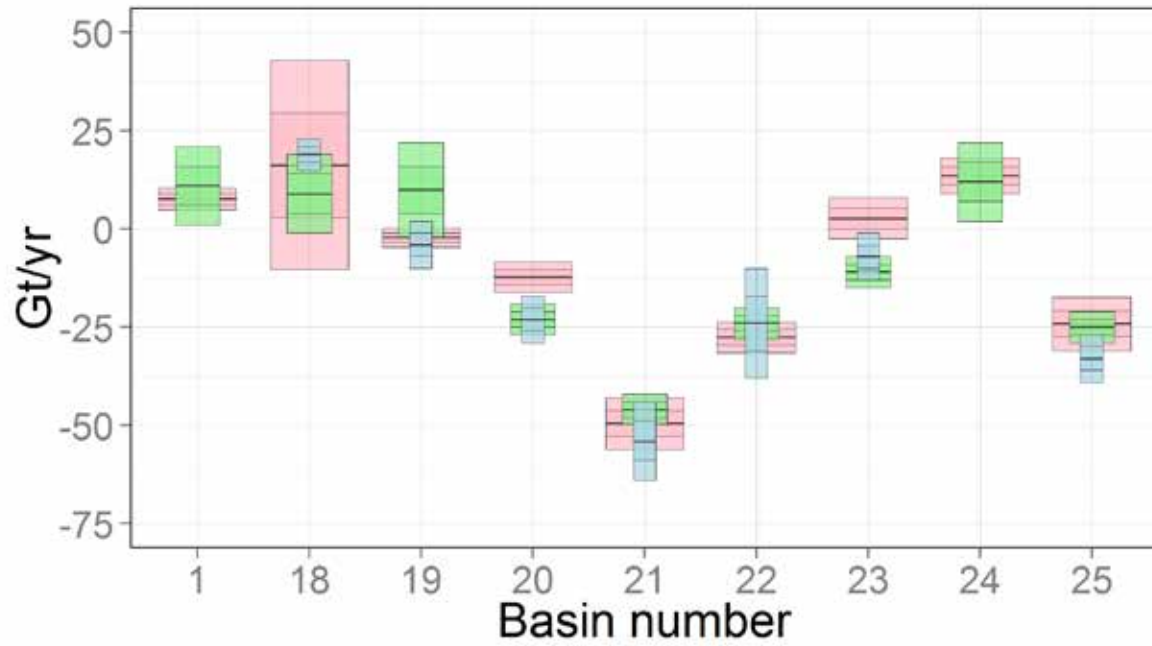
742 Figure 11. Basin definitions used for West Antarctica (adapted from Sasgen et al., 2013).



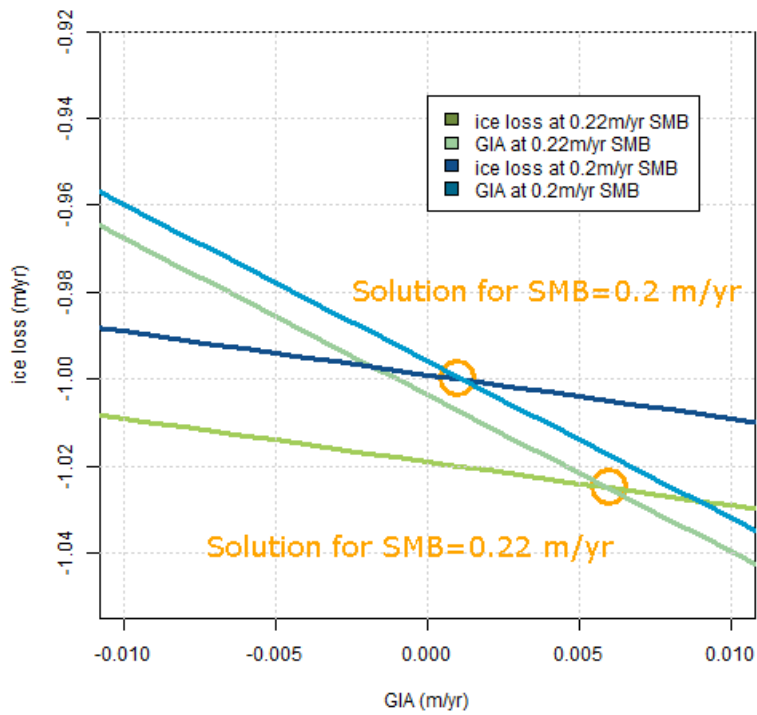
743

744 Figure 12. Comparison of RATES results with different GIA estimates and forward models.

745



746
 747 Figure 13. Combined Ice and SMB loss trends for West Antarctica using RATES (pink), results
 748 from King et al. (2013)(blue), and from Sasgen et al. (2013) (green). Basin definitions for King et
 749 al. (2012) differ for basins 1 and 24, so they are given in Table 3 instead. Our basin 25 is equal to
 750 the sum of basins 25 and 26 in King et al. (2012), this is given here as basin 25 for the King
 751 estimate.
 752
 753



754

755 Figure 14. Toy example illustrating the sensitivity of combination methods to differing SMB
 756 estimates. The blue lines represent the set of equations that solve for ice loss and GIA when
 757 SMB=0.2 m/yr. The green lines represent the equations for SMB=0.22 m/yr.

758

759 Table 1. GPS stations with vertical rate and errors, modelled elastic correction and adjusted rates.
 760 The latter are used for inference.

Site Name	Lat	Lon	Start Year	Start Day of year	End Year	End Day of year	data days	GPS rate (mm/yr)	Sigma	modelled elastic	adjusted GPS
ABOA	-73.04	346.59	2003	31	2010	11	1959	1.4	0.84	0.27	1.13
BELG	-77.86	325.38	1998	33	2005	45	1517	2.97	1.47	0.02	2.95
BREN	-72.67	296.97	2006	362	2010	194	463	3.85	1.6	1.85	2
FOS1	-71.31	291.68	1995	35	2010	364	317	2.14	0.4	1.64	0.5
MBL1_AV	-78.03	204.98						3.28	1.09	0.28	3
OHIG	-63.32	302.1	1995	69	2002	48	1667	3.8	1	NULL	3.8
PALM	-64.78	295.95	1998	188	2002	59	1181	0.08	1.87	NULL	0.08
ROTB	-67.57	291.87	1999	54	2002	59	239	1.5	1.9	NULL	1.5
SMRT	-68.12	292.9	1999	112	2002	59	751	-0.22	1.93	NULL	-0.22
SVEA	-74.58	348.78	2004	317	2008	20	1030	2.07	1.95	0.24	1.83
VESL	-71.67	357.16	1998	212	2010	328	3081	1.06	0.45	0.25	0.81
W01_AV	-87.42	210.57						-2.8	1.17	-0.09	-2.71
W02_AV	-85.61	291.45						2.17	1	0.28	1.89
W03_AV	-81.58	331.6						-2.47	1.28	-1.73	-0.74
W04_AV	-82.86	306.8						3.42	0.84	0.16	3.26
W04B/CRDI	-82.86	306.8	2002	358	2008	24	16	4.06	1.32	0.16	3.9
W06A	-79.63	268.72	2002	356	2005	358	12	-2.2	2.42	1.53	-3.73
W07_AV	-80.32	278.57						3.61	1.58	0.97	2.64
W09	-82.68	255.61	2003	9	2006	8	34	4.54	2.59	0.49	4.05
W12A/PATN	-78.03	204.98	2003	331	2007	363	17	6.41	1.61	0.28	6.13
W08A/B/SUGG	-75.28	287.82	2003	3	2006	4	13	1.31	1.28	1.3	0.01

761

762 Table 2. Prior information and soft constraints applied to length-scales and amplitudes based on
 763 expert judgement and analysis of the forward models discussed in section 2.4

Process	Length scale	Softly constrained amplitude (1sigma)	Dependency
GIA	3000 km	5mm/yr	Independent
Ice dynamics	50 km	1 mm/yr in interior – 15m/yr in areas flowing faster than ~15 m/yr	Independent
Firn compaction	80 km at coast – 200 km at interior	1 mm/yr in interior – 140 mm/yr at coast	Anti-correlated with SMB (rho = -0.4)
SMB	80 km at coast – 200 km at interior	1 mm/yr in interior – 240 mm/yr at coast	Anti-correlated with firn compaction (rho = -0.4)

764

765

766 Table 4. Mass trend values for each basin shown in Figure 8 for different values of the GIA length
 767 scale, SMB length scale and ice surface velocity threshold. All values in columns 2-4 are in Gt/yr.

Basin Number	Original mass trend	GIA length scale 1000 km	SMB length scale from RACMO: 150 km everywhere	Ice horizontal velocity threshold 50 m/yr
01	7.57 ± 1.41	7.49 ± 1.40	8.11 ± 1.36	5.40 ± 1.0
18	16.16 ± 13.26	13.48 ± 12.92	15.12 ± 13.05	24.80 ± 3.18
19	-2.24 ± 1.19	-2.23 ± 1.26	-2.18 ± 1.29	-0.71 ± 0.91
20	-12.22 ± 1.94	-11.47 ± 1.98	-12.28 ± 1.93	-13.21 ± 1.67
21	-49.48 ± 3.32	-45.31 ± 3.56	-49.53 ± 3.41	-47.01 ± 3.38
22	-27.62 ± 1.95	-26.34 ± 2.02	-27.34 ± 1.90	-24.12 ± 1.75
23	2.68 ± 2.65	3.28 ± 2.67	2.62 ± 2.65	-0.18 ± 2.59
24	13.57 ± 2.28	13.65 ± 2.30	13.39 ± 2.30	7.92 ± 1.67
25	-24.09 ± 3.39	-24.75 ± 3.20	-24.43 ± 3.42	-8.09 ± 1.90

768

769

770 Table 3. Ice and SMB mass trends from RATES, Sasgen et al. (2013), and King et al. (2012), in GT/yr. *Our basin 25 is equal to the sum of
 771 basins 25 and 26 in King et al. (2012). The sum of our basins 1 and 24 is equal to their sum of basins 1, 24, and 27.

Basin	RATES 03/2009- 10/2009	Sasgen (2013) 03/2009-10/2009	King (2012) 2002–2010	Diff RATES-Sasgen	Diff RATES-King
1	7.6	11	-	-3.4	-
18	16.2	9.5	19.2	6.7	-3
19	-2.2	10	-4	-12.2	1.8
20	-12.2	-23	-23	10.8	10.8
21	-49.5	-46	-54	-3.5	4.5
22	-27.6	-24	-24	-3.6	-3.6
23	2.7	-11	-7	13.7	9.7
24	13.6	12	-	1.6	-
25 (25+26)*	-24.1	-25	-33	0.9	8.9
(1+24+27)*	21.2	23	8.5	-1.8	12.7
WAIS	-75.5	-86.5	-117.3	9.2	41.8